SURFACE CHEMISTRY OF CARBON NANOPARTICLES FUNCTIONALLY SELECT THEIR UPTAKE IN VARIOUS STAGES OF CANCER CELLS

BY

INDRAJIT SRIVASTAVA

THESIS

Submitted in partial fulfillment of the requirements
for the degree of Master of Science in Bioengineering
in the Graduate College of the
University of Illinois at Urbana-Champaign, 2017

Urbana, Illinois

Adviser:

Professor Dipanjan Pan

ABSTRACT

Relationship of the surface physicochemical characteristics of nanoparticles with their interactions with biological entities may provide critical information for nanomedicinal applications. In this work, we have presented the systematic synthesis of sub 50nm carbon nanoparticles (CNP) presenting neutral, anionic, and cationic surface headgroups. A subset of CNPs with ~ 10, 20, and 40nm hydrodynamic sizes are synthesized with neutral surface headgroups.

The cellular internalization of these CNPs was systematically quantified for the first time in various stages of breast cancer cells (early, late and metastatic), providing a parametric assessment of charge and size effects. Distinct activities are noticed with these systems as they interact with various stages of the cancer cells. Our results indicated that a metastatic breast cancer could be targeted with a nanosystem presenting anionic phosphate groups. On the contrary, for patients with late stage cancer, drugs could be delivered with sulfonate functionalized carbon nanoparticles with higher probability of intracellular transport.

This study will facilitate a better understanding of nanoparticle-biologic interaction and the integration of this knowledge with pathophysiology would help to engineer nanomedicine with superior likelihoods to cross the endocytic “barrier” for delivering drug inside the cancerous cells.

Dedicated to my parents and my sister

ACKNOWLEDGEMENTS

First and foremost, I would like to express my sincere gratitude to my advisor Professor Dipanjan Pan for his excellent guidance, care and encouragement. I am grateful to him for providing me the continuous support I needed to continue powering through this project. Special thanks go to my mentor and coauthor Dr. Santosh Kumar Misra for his insightful discussions and great assistance in carrying out the experiments. I would also like to thank Jasleena Singh and Taylor Kampert for going over this thesis several times and giving their valuable comments.

Finally, I would like to thank my parents for allowing me to realize my own potential. All the support they have provided me over the years was the greatest gift ever bestowed on me. They also taught me the value of hardwork and dedication, without which, I may never have gotten where I am today.

TABLE OF CONTENTS

CHAPTER 1

INTRODUCTION

Myriad of nanoparticles have been developed for biological applications and a few of those have already been approved clinically to treat cancers. [1, 2] Despite some success, the unprecedented potential of nanomedicine has remained elusive. Failure in a clinical setup can be attributed to several factors, one of which is the lack of proper understanding of the mechanism of interaction of these agents with biological systems. [3-6] Relationship of the surface physicochemical characteristics of nanoparticles with their interactions with biological entities may provide critical information for nanomedicinal application.

Cellular internalization of nanoparticles is typically guided by penetration, adhesion, hemifusion and endocytosis. [7, 8, 9] Among these, endocytosis remains a fundamental feature of living cells, involved in several specialized functions, *e.g.* nutrients uptake, regulation of cell migration, immune system, etc. [10, 11] Endocytosis can be broadly classified into two mechanisms, phagocytosis and pinocytosis, [12-14] wherein the latter is the most common pathway utilized for entry in cells by the majority class of nanoparticles. It is known that endocytosis is dysregulated in cancer. Studies indicate that endocytotic alterations in cancer cells may affect cell surface expression of critical molecules and significantly influences the cancer-relevant phenotypes, with potential implications for interventions to control cancer by modulating nanoparticle surface chemistry and other parametric characteristics. It is now well recognized that various signaling pathways do persist in the endocytic route and emerging evidence ties endocytosis as a whole, or individual proteins to mitosis, apoptosis and cell fate determination.

Metastasis, for instance, is a multistep process requiring cancer cell signaling, invasion, migration, survival, and proliferation through dynamic modulation of cell surface proteins by endocytosis. Studies have shown that the internalization of nanoparticles in cells are often dictated by their size, [15, 16, 17] functionality, [18, 19, 20] and surface charge. [21, 22] However, the mechanistic understanding of nanoparticle internalization dependent on the stepwise progression of the cancer leading to tumor formation and subsequent metastatis, still lacks depth.

Our approach intends to borrow from the field of genetics to predict an individual's response to a drug based on the histopathological information obtained from biopsy. (Figure 1.1) This may result in a diagnostic cohort for stratification of 'right' nanomedicine candidate relying on cancer phenotypes for improved efficacy and reduced toxicity. Herein, we parametrically assess carbon nanoparticles based on size, charge and surface chemistry and stratify endocytic cellular uptake from pathophysiological differences. The choice of carbon as a nanoplatform was mainly chosen due to their ease of accessibility, low toxicity and facile surface chemistry. [23, 24] We report here the systematic synthesis of sub 50 nm carbon nanoparticles (CNP) presenting neutral, anionic, and cationic surface functionalities. A subset of CNPs with 10, 20 and 40 nm hydrodynamic sizes are also synthesized with neutral surface headgroups. The cellular internalization of these CNPs was systematically quantified for the first time in various stages of breast cancer cells (early, late and metastatic) providing a parametric assessment of charge and size effects.

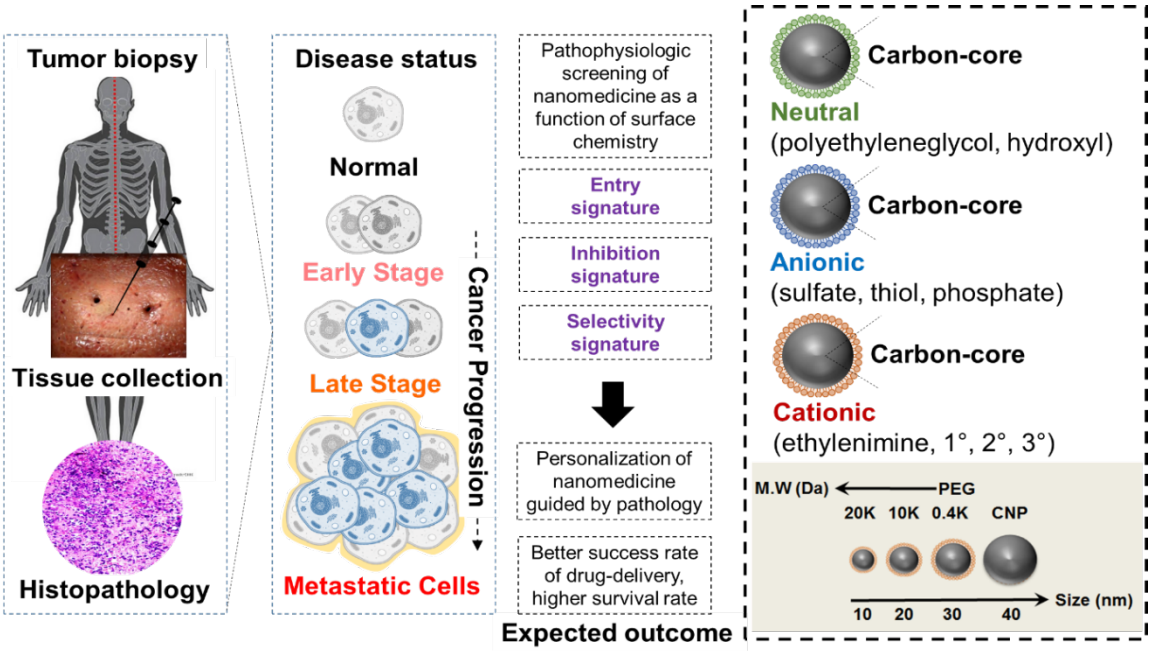

Figure 1.1 A schematic and conceptual representation of personalized selection of nanoparticles from pathophysiologic (tumor biopsy) and phenotype dependent (cancer stages) and its correlation as a function of surface chemistry and size.

A series of nanoparticles were prepared with cationic, anionic or neutral surface properties. It is now well established that endocytosis is a physiological process that is modified in cancer by significantly altering phenotypes. Although our knowledge remains limited and the pathophysiological contributions of these endocytic alterations may not be wholly understood, we decided to study the major endocytic routes, *i.e.* clathrin, lipid-raft mediated, dynamin, and energy dependent pathways. Our results demonstrated fort he first time that carbon nanoparticles, as a function of their surface charge and particle diameter, typically favor a selective endocytic pathway depending on the progression of breast cancer. This understanding of surface characteristics and cancer stage-driven internalization of particle may improve the success of nanotherapy with minimum cytotoxicity and maximum selectivity.

CHAPTER 2

EXPERIMENTAL METHODS

2.1 MATERIALS

Agave nectar (18% glucose and 56% fructose by weight, Honey Tree's® Organic Agave Nectar, MI, USA) was obtained from a local grocery store. Poly (ethylene glycol) (PEG, average M_n = 400, M_n =10,000 and M_n= 20,000), Polyethylenimine, branched (PEI, average $M_w \approx 25{,}000$), Sucrose (≥99.5%), Sodium azide (NaN_3, ≥99.5%), Nystatin, 2-Deoxy-D-Glucose (DOG, ≥98%) were purchased from Sigma-Aldrich (MO, USA) and used without further purification. Polyethylene glycol phosphate (PO_4-, Mw=5000) was purchased from Chemicell (Berlin, Germany). Methoxy PEG Thiol (SH, ≥97%, M_w= 20,000) was purchased from JenKem Tech. (TX, USA). Polyethylene glycol monomethyl ether mesylate (SO_3H, Mw=5000) and Chlorpromazine (CPM, 97%) were purchased from Santa Cruz Biotechnology (TX, USA). Dynasore (>99%) was purchased from Fisher Scientific (PA, USA). The 0.2 μM and 0.45 μM filters (Millex, Merck Millipore Ltd., Tullagreen, Carrigtwohill, County Cork, Ireland) were used wherever applicable.

2.2 PREPARATION OF CARBON NANOPARTICLES

Pristine CNPs were prepared by dissolving 250 mg of agave nectar in 2 ml of nanopure water (0.2 μM, 18 MΩ·cm). Then the aqueous solution was heated on a hot plate at 270 °C for roughly 30 mins and re-suspended in 4 ml of nanopure water. Followed by 20 min probe sonication (Q700^{TM}, Qsonica Sonicators, CT, USA) (Amp:1, On: 2 sec, Off: 1 sec), the solution was passed

through a syringe filter with a 0.2 μm pore size (Millex®, Merck Millipore Ltd., County Cork, Ireland) prior to use.

2.3 PREPARATION OF CARBON NANOPARTICLES BY PRE-PASSIVATION

A mixture of agave nectar and polymer (PEGylated CNPs, CNP PO_4, CNP SO_3H, CNP SH) was taken in glass sample vial of 20 mL capacity. To this, nanopure water was added and solution was mixed well to form a homogenous mixture. The concentration ratio of agave nectar to polymeric passivating agent was maintained at 1:1 (w/w). For the nucleation process, a hot plate surface was maintained at 270 °C while glass vials were kept un-capped to allow the slow evaporation of water. The temperature was maintained for around 30 mins, which led to generation of brownish to black mass (varies with passivating agent). The reaction mixture changed color from light yellow to dark brown to black along the course of the heating process. The as-synthesized particle mass was suspended in 4 mL of nanopure water followed by 20 min probe-sonication (Q700^{TM}, Qsonica Sonicators, CT, USA) (Amp: 1, on: 2 sec, off: 1 sec). Sonicated suspension was centrifuged at 12000 g for 20 min, followed by collecting the supernatant by filtering through a 0.22 μm syringe filter.

2.4 PREPARATION OF CARBON NANOPARTICLES BY POST-PASSIVATION

In order to make CNP-PEI, 10 μL of branched PEI solution (1mg/10μL) were added to 1 mg of CNPs. After vortexed and left at room temperature for 30 mins, the solution was centrifuged for 30 min at 75,000 rpm at 4 °C (Optima^{TM} MAX-XP Ultracentrifuge, Beckman-Coulter, CA, USA) to remove the suspension. The collected pellet was then redispersed in nanopure water and

probe-sonicated for 2 mins (Amp: 1, On: 2 sec, Off: 1 sec). All CNP formulations were made same concentration (5mg/ml) before using for the study.

2.5 DYNAMIC LIGHT SCATTERING

The hydrodynamic size distribution of the nanoparticles was determined through dynamic light scattering measurements on Malvern Zetasizer ZS90 instrument (Malvern Instruments Ltd, United Kingdom) at fixed angle of 90^{o}. A 10 µL of particle suspension was mixed with 990 µL of nanopure water to run the samples in DLS machine. A photomultiplier aperture of 400nm was used and the incident laser power was so adjusted to obtain a photon counting rate between 200 and 300 kcps. Measurements for which the measured and calculated baselines of the intensity autocorrelation function were within 0.1% range were used for diameter values. All measurements were carried out in triplet of thirteen consecutive measurements.

2.6 TRANSMISSION ELECTRON MICROSCOPY

Prior to sample preparation of CNP's for TEM imaging, the nanoparticles were mildly vortexed. A 10 µL of nanoparticle sample (~0.1 mg/mL) was drop cast on 200-mesh copper grid. After waiting for 1 min, the excess fluid was absorbed by lint free Kim wipes. The transmission electron micrographs were acquired on a JEOL 2100 Cryo TEM machine and imaged by Gatan UltraScan 2k × 2k CCD camera.

2.7 ZETA POTENTIAL MEASUREMENTS

Zeta potential (ζ) values were determined using a Malvern Zetasizer (Malvern Instruments Ltd, United Kingdom) of Nano series. The experiments were performed at 25°C and pH 7 at the light scattering mode in the phase analysis light scattering (PALS) mode following solution equilibration at 25 °C. Calculation of ζ from the measured nanoparticle electrophoretic mobility (μ) employed the *Smoluchowski equation*: $\mu = \varepsilon\zeta/\eta$ where ε and η are the dielectric constant and the absolute viscosity of the medium, respectively. Measurements of ζ were reproducible within ±2 mV of the mean value, given by 3 determinations of 15 data accumulations.

2.8 UV-VIS AND FLUORESCENCE MEASUREMENTS

Ultraviolet-visible (UV-Vis) absorbance of CNPs was recorded on GENESYSTM 10S UV-Vis Spectrophotometer (Thermo Scientific, MA, USA). Absorbance spectra were collected at an interval of 1 nm scanning from 200–900 nm. The emission spectra of fluorescence measurements were obtained through NanoDrop 3300 Fluorospectrometer (Thermo Scientific, MA, USA). The excitation wavelength was set to 365 nm and the wavelength covered an excitation range between 430 nm and 800 nm.

2.9 RAMAN AND FT-IR MEASUREMENTS

Aqueous suspension of the nanoparticles was dried onto a MirrIR IR-reflective glass slides (Kevley Technologies, Chesterland, Ohio, USA) for Fourier Transform Infrared (FT-IR) measurements using a Nicolet Nexus 670 FTI-IR (Fredrick Seitz Material Research Laboratories (FSMRL), Urbana, Illinois, USA). For each measurement $100 \times 100\,\mu$m images were collected at $1\,cm^{-1}$ spectral resolution with 64 scans per pixel and a $25 \times 25\,\mu$m pixel size and individual spectra were corrected for atmospheric contributions. Raman spectra were acquired through dried samples described in the Infrared spectroscopy section in a reflection mode of Nanophoton Raman-11 (FSMRL). The excitation wavelength for all measurements was 532 nm and the power was set to 2% with a 60 s acquisition time. The Raman shift from 400 to $4000\,cm^{-1}$ was collected at $1\,cm^{-1}$ spectral resolution while the Laser light was focused through a 20× objective.

2.10 NMR MEASUREMENTS

^{1}H NMR measurements were performed on VARIAN UNITY 500 (Varian, Inc., Palo Alto, CA) spectrometer operating at 500 MHz equipped with 5 mm Nalorac QUAD probe. Chemical shifts were reported in ppm and referenced to the solvent proton impurities. Deuterium oxide (D_2O) was used as the deuterated solvent for all the used samples. A 600 µl of sample was transferred to the NMR tube for acquiring chemical shifts. A total of 256 acquisitions were made and the data was processed and analyzed with MestRenova™ 8.1 software (Mestrelab Research SL; Santiago de Compostela, Spain).

2.11 CONFOCAL MICROSCOPY STUDIES

MCF-7 cells were plated on circular 22 mm glass microscope slides at a cell density of 400,000 cells/slide in a volume of 200 μL of growth medium and placed in a six-well plate. The cells were incubated at 37 ˚C and 5% CO_2 for 24 hours prior to treatment. The cells were washed twice with 1 ml of reconstituted medium and treated with a 10% v/v solution containing 100 μL of nanoparticle formulation and 900 μL of DMEM with 10% FBS. Following 4 hours of incubation, the cells were washed twice with DPBS, fixed with 4% w/v paraformaldehyde in DPBS, and mounted onto glass slides with DAPI-containing mounting medium. The confocal microscopy measurements were taken on the Zeiss LSM 700 (Peabody, MA, United States) and the samples were excited at 488 nm for the DAPI and 555 nm and 639 nm for the CNP measurements using suitable filters.

2.12 MTT ASSAY

The cytotoxic effect of various CNPs in different breast cancer cell-lines were investigated with a 3-(4,5-dimethylthiazole-2-yl)-2,5-diphenyltetrazolium bromide (MTT) assay (Sigma-Aldrich, MO, USA). MCF-7, MDA-MB231, BT-549 and MCF-10a cells were plated in a 96-well plate at a density of 10,000 cells per well (Greiner Cellstar® 96 well plates, Sigma-Aldrich, MO, USA) and were allowed to grow for 24 h at 37 °C to reach around 80-85% cell confluence. Grown cells were then exposed with CNPs whose concentration was ranging from 10, 5, 2.5, 1.25, 0.625, 0.31 and 0.15% (v/v). Followed by a 44 h exposure time, 20 μL (5 mg/mL) of MTT solution was added to each well and cells were further incubated for another 4 h. After incubation, media were aspirated and 200 μL of dimethyl sulfoxide

(DMSO, ≥99%, MP Biomedicals, USA) was added to dissolve formazan crystals. Optical density of the samples was determined by Synergy HT (BioTek, USA) with a reference wavelength of 592 nm. The percentage cell viability was determined by the following equation:

% Cell viability = [{(A592 treated cells) − (A592 background)} / {(A592 untreated cells) − (A592 background)}] x 100

2.13 MIXED CELL CULTURE

MCF-7 and MDA-MB231 cells (8000 per well) were mixed together in different percentages (50:50, 25:75 and 75:25) and plated in a 96 well plates. Cells were grown for 24h before being incubated with different endocytic inhibitors. Cells were incubated with inhibitors and CNPs as described above. All the treatments were performed in triplicate. At the end of the incubation period, growth media were aspirated and 200 μL of dimethyl sulfoxide (DMSO, ≥ 99%, MP Biomedicals, USA) was added to dissolve formazan crystals. Absorption of the samples was determined by Synergy HT (BioTek, USA) with a reference wavelength of 592 nm.

% Cell viability = [{(A592 treated cells) − (A592 background)} / {(A592 untreated cells) − (A592 background)}] x 100

2.14 INHIBITOR STUDIES

MCF-7, MDA-MB231, BT-549 and MCF-10a cells (10^5) were plated in 96 well plates. Cells were grown for 24h before being incubated with different endocytic inhibitors. Inhibitor formulations were made with reconstituted medium having sodium azide, DOG (deoxyglucose), CPM (chlorpromazine), Nystatin and Dynasore at a concentration of 10 μM, 50 μM, 28 μM, 180 nM and 80 μM, respectively, which were used as described in some previous reports [41,42,43]. Cells were incubated with inhibitors for 1h at ambient condition. Inhibitors were then replaced with CNPs suspensions in reconstutited medium at concentrations of 5% (v/v). All the treatments were performed in triplicate. Cells that had only inhibitor treatments were considered as negative controls whereas cells treated with only CNP formulations without any pre-inhibitor treatment were used as positive controls. The cytotoxic effect of CNPs were investigated with a 3-(4,5-dime thylthiazole-2-yl)-2,5-diphenyltetrazolium bromide (MTT) assay (Sigma-Aldrich, MO, USA). Cells were further grown for 44 h and at the end of incubation, a 20 μL (5 mg/mL) of MTT solution was added to each well and cells were further incubated for another 4.5 h. After incubation, media were aspirated and 200 μL of dimethyl sulfoxide (DMSO, ≥ 99%, MP Biomedicals, USA) was added to dissolve formazan crystals. Absorption of the samples was determined by Synergy HT (BioTek, USA) with a reference wavelength of 592 nm.

% Cell viability = [{(A592 treated cells) − (A592 background)} / {(A592 untreated cells) − (A592 background)}] x 100

2.15 ENDOCYTIC BLOCKERS TO STUDY CELL INTERNALISATION OF CNPs

Response to cellular entry of CNPs against endocytic blockers were studied by fold decrease in cell death or increase in cell viability. It measures how the cell viability values for different CNP formulations, changed with/without the presence of inhibitors. The values were calculated by the following formula:

Fold increase in Cell viability = ((Cell viability of CNP in presence of inhibitor – Cell viability of CNP in absence of inhibitors) / Cell Viability of CNP in absence of inhibitors)

2.16 STATISTICAL ANALYSIS

Statistical analysis on various biological results was carried out by using one-way ANOVA method. CNP Pristine was treated as control and compared to other CNP formulations. Fold increase for the nanoparticle formulations was plotted as mean values ± standard deviation, n = 3. Statistical analysis results were represented as * for $p<0.05$, ** for $p<0.01$, *** for $p<0.001$ and **** for $p<0.0001$.

CHAPTER 3

RESULTS AND DISCUSSIONS

3.1 CARBON NANOPARTICLES SYNTHESIS

In this work, CNPs were prepared using two different strategies which included pre-and post-passivation. [23] In both of these techniques, the carbon core was synthesized from the agave nectar, a natural carbohydrate mainly containing glucose, fructose, and other carbohydrate sources. The surface of the carbon core was passivated with either linear (PEG's) or branched (PEI, etc.) organic macromolecules for the synthesis of both pre- and post-passivated nanoparticles. Macromolecule passivated carbon nanoparticles (CNP), along with pristine CNPs were characterized by physico-chemical techniques.

3.2 PHYSIOCHEMICAL CHARACTERIZATIONS

Figure 3.1 A, B depict the distribution of hydrodynamic diameter of CNPs and the corresponding data has been summarized in Table 3.1 calculated from the dynamic light scattering (DLS) measurements. It was interesting to note that PEGs, PO_4, SO_3H, SH and PEI passivated CNPs exhibited their hydrodynamic diameter in the range of 8-40 nm. This could be due to the possible cloaking of the polymer around the carbon core. In addition to DLS measurements, Transmission electron microscopy (TEM) was performed on the pristine and passivated CNPs to analyze their

anhydrous state morphologies. Representative TEM images for CNP, CNP PO_4, CNP SH, CNP PEG400 and CNP PEG20K shows a sub-50 nm spheroidal morphology as shown in Figure 3.2.

Nanoparticles	Hydrodynamic Diameter (nm)	Zeta Potential (mV)
CNP Pristine	49±10	-22±01
CNP PEG400	33±09	-20±05
CNP PEG10K	17±04	-08±01
CNP PEG20K	08±01	-11±01
CNP PEI	41±04	+19±02
CNP PO_4	26±07	-11±02
CNP SO_3H	25±10	-21±02
CNP SH	28±08	-06±02

Table 3.1 Dynamic light scattering analysis and zeta potential measurements of different CNPs and the results are arranged as mean ± standard deviation.

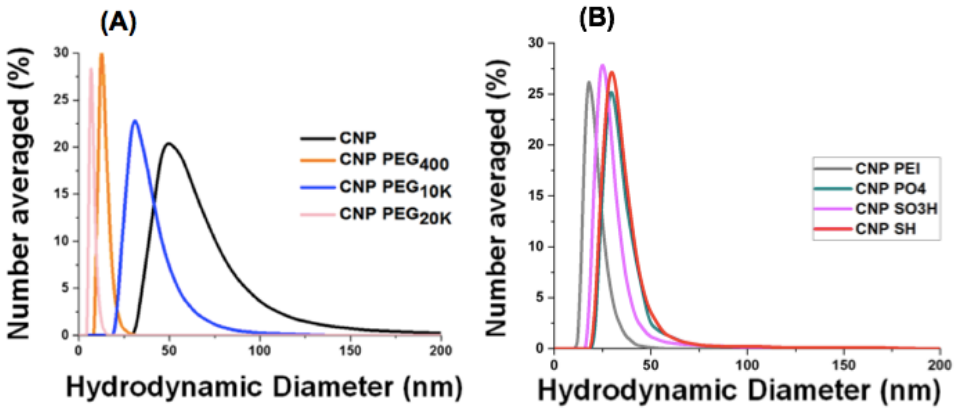

Figure 3.1 (A, B) Hydrodynamic size distribution for pristine CNP and passivated CNPs using dynamic light scattering.

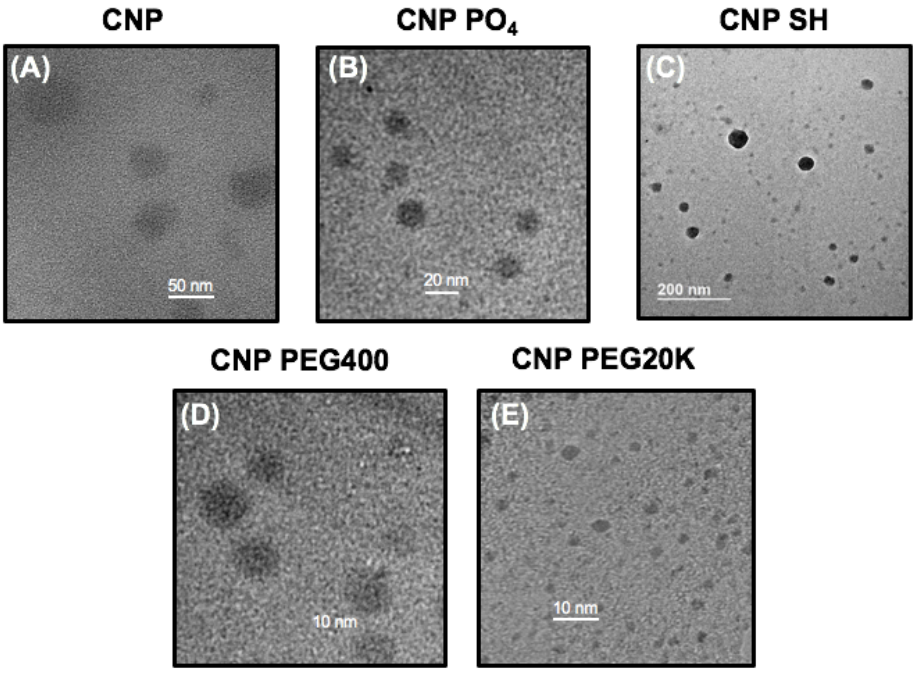

Figure 3.2 Transmission electron micrographs of the prepared nanoparticles; (A) CNP, (B) CNP PO_4, (C) CNP SH, (D) CNP PEG400 and (E) CNP PEG20K.

UV-Vis absorption spectra of pristine and passivated CNPs were carried out in the range of 250-750 nm as shown in Figure 3.3. The characteristic strong peak in pristine CNP appeared at ~280 nm along with a weak broad peak at 350 nm. Interestingly, this absorption spectrum remained more or less unaltered in CNP passivated by anionic polymers. On the contrary, 280 nm peak of CNP tends to become much broader/distorted when passivated with cationic polymers. A further investigation is needed to understand the exact effect of surface passivation over the absorption response of CNPs. The fluorescence measurements were carried out by exciting the synthesized CNP's at 360 nm (λ_{ex}) and tracking their emission from 430 to 800 nm (λ_{em} range). Figure 3.4 showed the high fluorescence intensity of pristine CNP which gets reduced when it's passivated with either anionic or cationic polymers. Interestingly, fluorescence intensity of CNPs passivated with macromolecules exhibiting negative surface charge (PO_4) were much higher compared to CNP's passivated with macromolecules with positive surface charges (PEI). Such observation could be attributed to the different surface chemistries on the nanoparticle surface.

The negative zeta potential on the surface of pristine CNP (no surface coating or passivating agent) could be attributed to the presence of over-abundance of carboxyl, hydroxyl and carbonyl groups on its surface as shown in Figure 3.5 and Table 3.1. Subsequent passivation of pristine CNP with polymer macromolecules (linear or branched) lead to an increase in its zeta potential value. A negative zeta potential was reported for CNP's passivated with neutral or anionic polymers (PEG's, PO_4, SO_3H, SH) however, CNP's passivated with cationic polymers (PEI) exhibited positive zeta potential values. It supported the hypothesis that retention of macromolecule charge occurs during preparation procedure of CNPs.

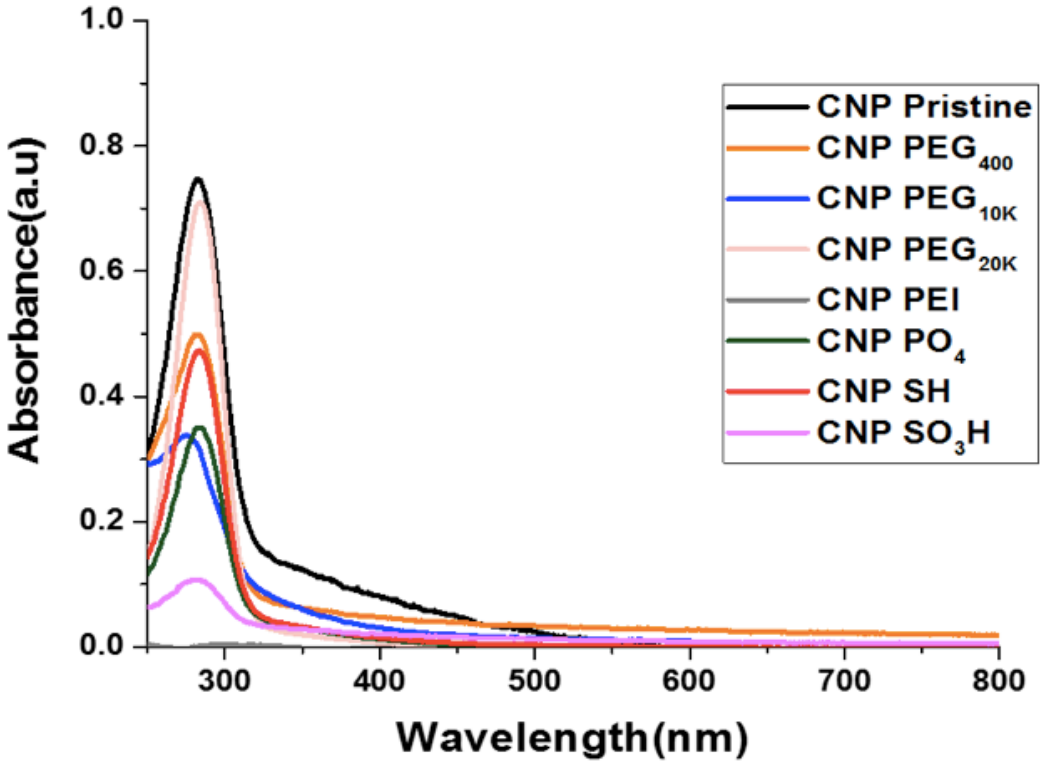

Figure 3.3 UV-Vis spectroscopic measurements for pristine and passivated CNPs. The characteristic strong peak in pristine CNP appeared at ~280 nm along with a weak broad peak at 350 nm. Interestingly, this absorption spectrum remained more or less unaltered in CNP passivated by anionic polymers. On the contrary, 280 nm peak of CNP tends to become much broader/distorted when passivated with cationic polymers. A further investigation is needed to understand the exact effect of surface passivation over the absorption response of CNPs.

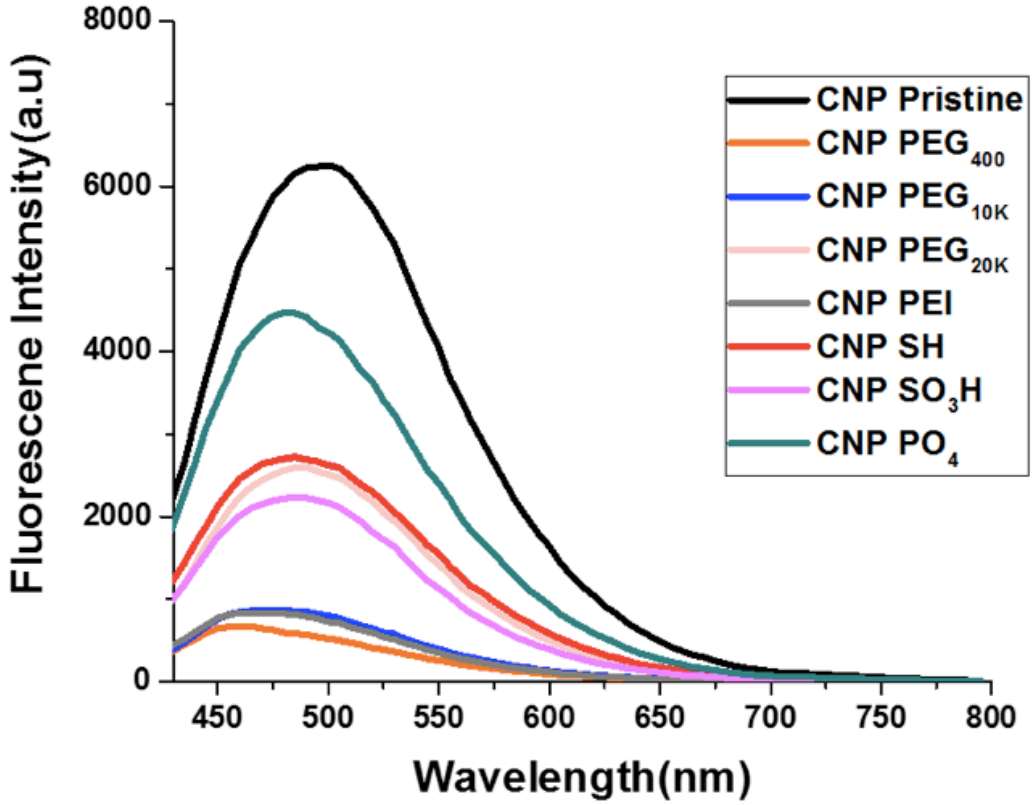

Figure 3.4 Fluorescent measurements for bare and functionalized CNPs. The fluorescence measurements were carried out by exciting the synthesized CNP's at 360 nm (λ_{ex}) and tracking their emission from 430 to 800 nm (λ_{em} range). It showed high fluorescence intensity of pristine CNP which is reduced when it is passivated with either anionic or cationic polymers. Interestingly, fluorescence intensity of CNPs passivated with macromolecules exhibiting negative surface charge (PO_4) was much higher compared to CNP's passivated with macromolecules with positive surface charges (PEI). Such observation could be attributed to the different surface chemistries on the nanoparticle surface.

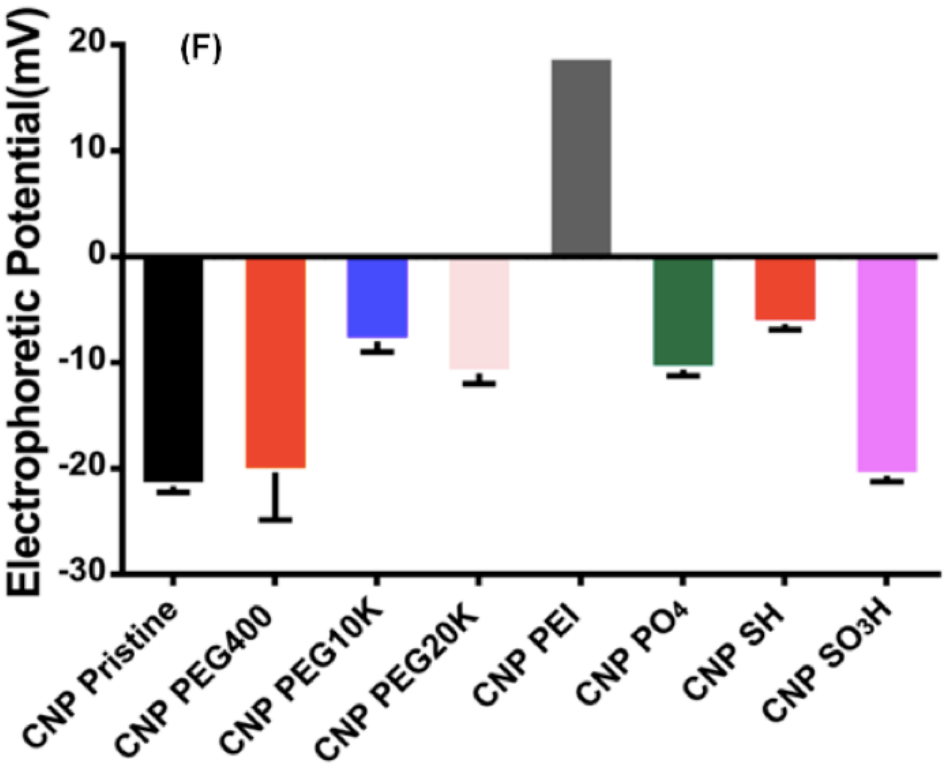

Figure 3.5 Electrophoretic zeta potential measurements for pristine and passivated CNPs prepared via pre- and post-passivation routes.

For accessing the surface chemistry of CNPs, Raman and FT-IR spectroscopic studies were performed. A Raman spectra of amorphous carbon materials is usually characterized by the presence of 'G' (*graphitic*) and 'D' bands (*disordered graphitic*) bands.[24] The D band (sp^3 hybridized) is often referred to as the disorder band or the defect band and is associated with the vibration of carbon atoms with dangling bonds in the terminal plane of the disordered graphite of amorphous carbon. The G band (sp^2 hybridized), on the other hand, is related to the vibration of carbon atoms in a two dimensional hexagonal lattice. The ratio of the intensities of the two parameters (I_G/I_D) is used here as an indicator for the determination of the structure of CNPs.

Raman spectra of pristine CNP and functionalized CNP's (Figure 3.6A) showed that I_G/I_D ratio is highest for pristine CNP and eventually falls down when coated with polymer macromolecules. It was also interesting to note that I_G/I_D ratio is greater than 1 in CNP passivated with some anionic polymers (PO_4^-, SO_3H, SH) which clearly indicated the presence of more graphitic domains over diamond-like domains. In contrast, I_G/I_D ratio falls below 1 in CNP passivated by cationic polymer (PEI), due to the presence of more diamond-like domains over graphitic domains.

FT-IR spectra of Pristine and passivated CNP's were obtained as shown in Figure 3.6B. From the infra-red spectrum of Pristine CNP, we notice a broad peak that is centered around 3450 cm^{-1}. It also exhibits asymmetric stretching band, which corresponds to methyl functionalities (νaCH_3) at at 2900 cm^{-1} and methylene stretching band (νsCH_2) at 2820 cm^{-1}. We also observe the C=O stretching band is obtained at 1750 cm^{-1}. The presence of hydrophilic groups on its surface results in an increased aqueous suspendability. Furthermore, passivated CNP's were found to display spectra which included features of both the carbon core as well as the macromolecule with which it was passivated. We also observed carbonyl stretching (–C=O) and broad O-H and S-H vibrations for CNP SH and C-H (stretch and bend), carbonyl stretching (-C=O), S-H stretch and narrow O-H vibrations for CNP SO_3H. For CNP PO_4, a C-H and PO_4^{3-} stretching and with narrow O-H vibrations and for CNP PEG20K, broad O-H vibrations and C-H, C-O, C-O-C stretching was observed.

Surface chemistries were further confirmed by ^1H NMR spectroscopy studies. Experiment was carried out on the 500 MHz machine using a representative nanoparticle system CNP-SO_3H. NMR peaks for the passivating macromolecules (Figure 3.7 and Figure 3.8**)** compared with data from literature report. [25,26] In addition, a spectrum for the Pristine CNP was obtained to use as

control spectrum to compare with passivated CNP. It was clearly observed that the chemical features from PEG SO_3H have remained intact even after carbonization, confirming that the moieties could effectively function in the follow- up experiments.

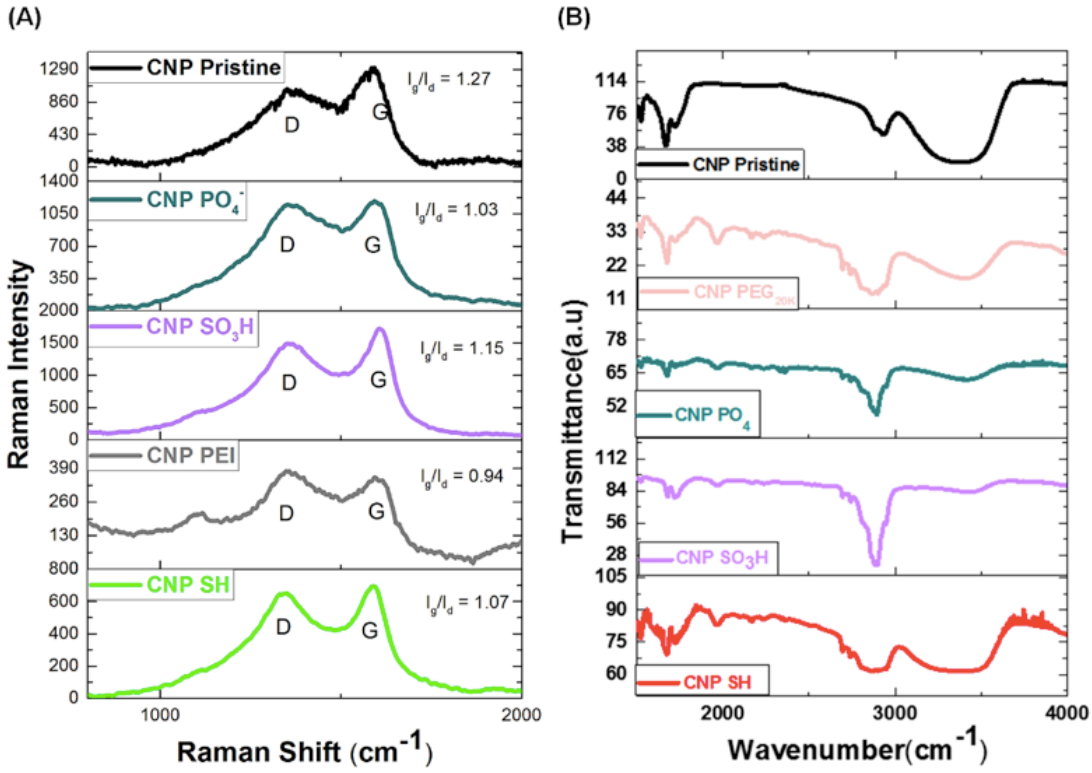

Figure 3.6 (A) Raman spectra of pristine CNP and CNPs passivated with PO_4, SO_3H, PEI and SH respectively; (B) FT-IR spectra of pristine CNP and CNPs passivated with PO_4, SO_3H, PEG and SH respectively.

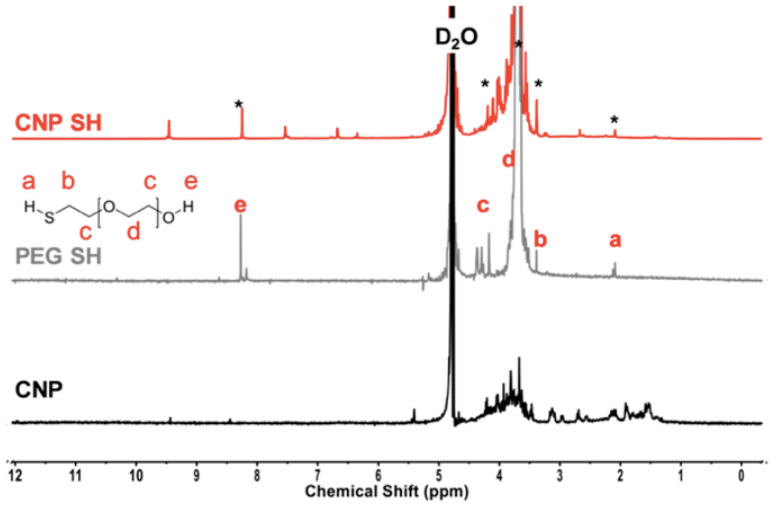

Figure 3.7 ^{1}H-NMR spectra of CNPs, comparing parent macromolecule PEG SH with surface passivated CNPs (CNP SH) showing the retention of peaks from PEG SH (marked with the black stars) while the blue stars indicate the features maintained from CNPs.

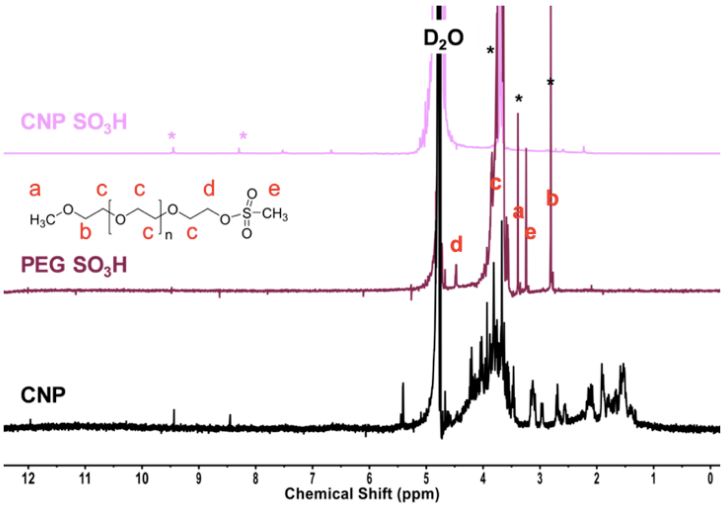

Figure 3.8 ^{1}H-NMR spectra of CNPs, comparing parent macromolecule PEG SO_3H with surface passivated CNPs (CNP SO_3H) showing the retention of peaks from PEG SO_3H (marked with the black stars) while the purple stars indicate the features maintained from CNPs.

3.3 MECHANISMS OF CELLULAR ENTRY IN CELLS OF DIFFERENT CANCER STAGES

Cellular toxicity of CNPs in non-tumorigenic breast cells and tumorigenic breast cancer cells lines were evaluated by using MTT Assay (Figure 3.9). It works on the premise that decrease in mitochondrial respiration can be directly correlated to decrease in live cell population. This respiration eventually leads to mitochondrial oxidation, following which an added MTT reduces to form blue colored crystal of formazan. Concentration of the produced formazan crystals are found to be directly proportional to live population of cells, which gets decreased when cellular toxicity of CNPs increase. It was found that non-passivated CNPs do not have any considerable selectivity toward any of the used cell lines. Experiments were performed using CNPs at a concentration of 5% (v/v) with reconstituted growth medium. Cellular toxicity of nanoparticles generally correlates with delivered amount to intracellular compartment. The efficiency of being taken up and their routes for cellular entry can be used to analyze surface chemistry correlation for various CNPs to different stages of breast cancer. Results from the study would be able to generate a library of surface chemistries beneficial to deliver therapeutics using CNPs in different stages of cancer which could probably be extrapolated to other nanoparticle systems too. Studies were performed by blocking the selective endocytic entry path followed by CNP treatment to observe after effect of cellular entry of CNPs. Uptake of CNPs in MCF-10A (non-tumorigenic breast cell line), MCF-7 (early stage breast cancer cell line), MDA-MB231 (late stage breast cancer cell line), BT-549 (metastatic breast cancer cell line) and heterogeneous mixture of MCF-7 and MDA-231 cells at ratio of 25:75, 50:50 and 75:25 were used to verify the route of cellular entries and their variation from non-cancer to different stages of cancers. Use of normal breast cells facilitates the comparison profile which would provide a background on the uptake mechanisms of CNPs. Pharmological inhibitors of the cellular entry pathways were used

for uniform, quantified effect on all cell populations and have no considerable toxicity in short period incubations. They also and do not affect the actin cytoskeleton post treatment. [27,28] It was anticipated that a particular inhibitor would block a specific endocytic route of entry and consequently any CNPs entering the cells *via* that pathway. This in turn would decrease the cell internalization and subsequently increases the overall viability of the cell.

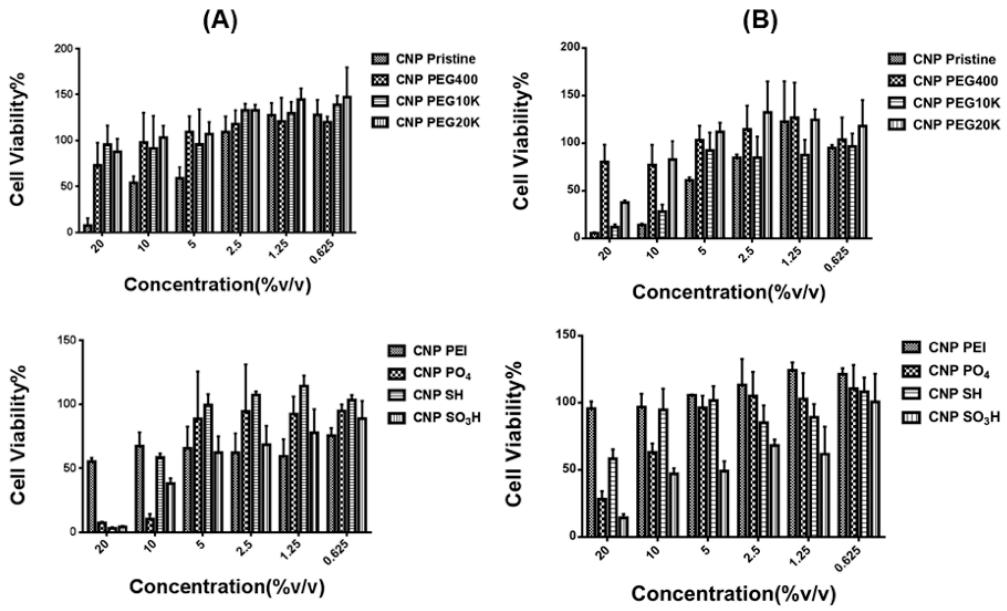

Figure 3.9 (a) MTT Assay for evaluation of cytotoxic effects of pristine CNP and functionalized CNP's in (A) MCF-10A, non-tumorigenic breast cells; (B) MCF-7 breast cancer cells. Experiments were performed in the above cell-lines after incubation for 48 h at various concentrations (20, 10, 5, 2.5, 1.25 and 0.625 %v/v).

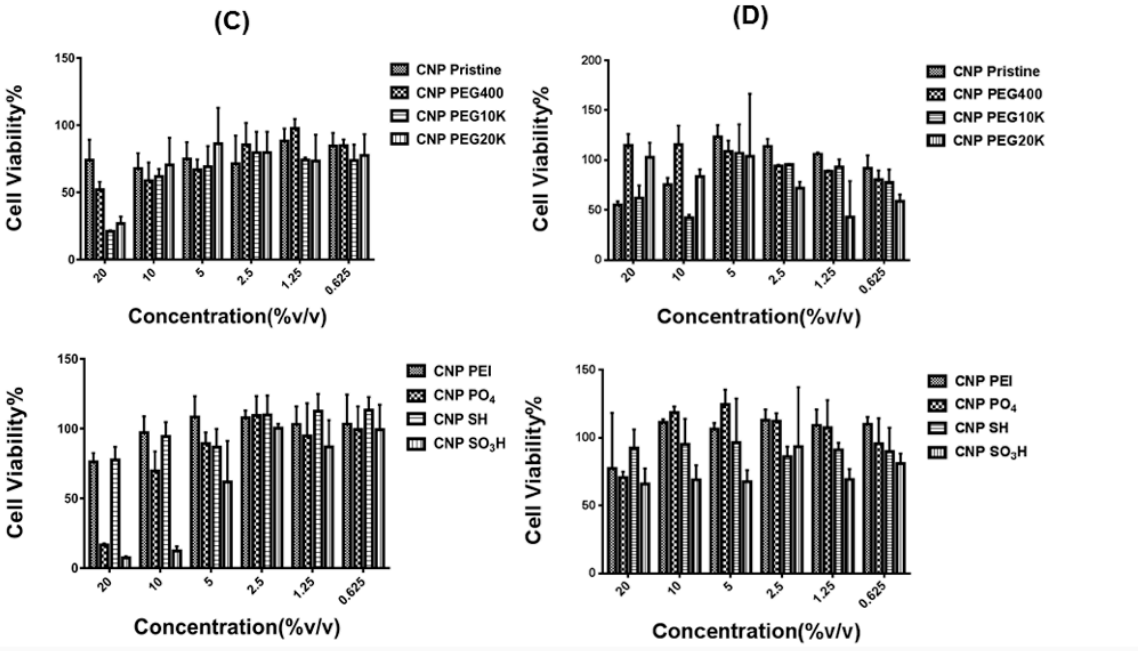

Figure 3.9 (Cont.) (b) MTT Assay for evaluation of cytotoxic effects of pristine CNP and functionalized CNP's in (C) MDA-MB231 breast cancer cells; (D) BT-549 breast cancer cells. Experiments were performed in the above cell-lines after incubation for 48 h at various concentrations (20, 10, 5, 2.5, 1.25 and 0.625 %v/v).

Learning this expected behavior of cells post incubation, inhibitors with different functions were used. It included a mixture of sodium azide (NaN_3) and 2-deoxyglucose (DOG), which helped in inhibiting glycogenosis and cellular respiration respectively *via* energy dependent uptake.[29,30,31] The analysis of clathrin dependent entry was outlined using Chlorpromazine (CPM), a cationic amphiphilic drug. It was supposed to reduce the formation of clathrin-coated pits due to a reversible translocation of clathrin and its adapter proteins from the plasma membrane to intracellular vesicles. [32,33,34] Dynasore has been used to understand the inhibition of dynamin (GTPase) dependency in endocytosis of cells.[35,36] Finally, Nystatin, a sterol-binding agent,

which dismantles caveolae and cholesterol in the membrane, has been employed to study clathrin-independent inhibition of endocytosis.[37,38]

To investigate the mechanism of entry 10 x 10^3 cells were plated in a 96 well plate for 24h and allowd to reach a confluency of around 80%. Cells were further incubated with various inhibitors for 1h (Table 3.2). Cells were incubated with solution of NaN_3 (10 mm) and DOG (50 mM) or CPM (28 nM), Nystatin (180 nM) and Dynasore (80 μM) for 1h. Cell medium was further replaced with 5% (v/v) of CNPs in respective reconstituted medium for 48h before performing the MTT assay. Particular attention was given to parametric assessment as a function of surface charge and nanoparticle hydrodynamic radii to understand their signature in entry, selectivity or inhibitory routes.

Table 3.2 Inhibitors and their treatment conditions for achieving endocytic inhibition by defined working mechanism.

Endocytic inhibitors	**Working mechanism**	**Working concentration**	**Incubation time**
NaN_3 / DOG (37°C)	ATP depletion	10 mM / 50 mM	1h
NaN_3 / DOG (4°C)	ATP depletion + slows down metabolism	10 mM / 50 mM	1h
CPM	Inhibits clathrin mediated endocytosis	28 nM	1h
Nystatin	Inhibits lipid-raft mediated endocytosis	180 nM	1h
Dynasore	Inhibits dynamin-dependent endocytosis	80 μM	1h

For non-cancerous breast cells (MCF-10A), CNP passivated with a cationic or anionic polymer (PEI, -SH, -SO_3H, -PO_4) followed predominantly a clathrin-mediated internalization pathway. (Figure 3.10) Study was extended to primary stage breast cancer cells (MCF-7), and was found that lower molecular weight (M_w) PEGylated CNP (CNP PEG_{400}), entered the cells *via* energy dependent pathway, clathrin-mediated pathway and dynamin-dependent pathway while higher M_w PEGylated CNPs (CNP PEG_{10K}, CNP PEG_{20K}) preferred entering the cells via clathrin-mediated pathway. Interestingly, a high level of selectivity was noticed for CNP SO_3H, which was found to be internalized *via* energy dependent pathway. (Figure 3.11) However, it was found that none of the remaining positively, negatively or neutral CNPs favored any of the investigated pathways.

In order to confirm that endocytic inhibitors are truly in function, the incubation temperature was lowered to 4°C while incubating cells with NaN_3/DOG. This alteration expectedly resulted in lowering of the efficacy of the inhibitor, which consequently led to an increase in cellular entry compared to physiological temperature (37 °C). In the case of PEGylated CNPs, lowering the temperature resulted in a further increase of cellular entry for only CNP PEG_{10K} while no effect was noticed for CNP PEG_{400} and CNP PEG_{20K}. The rest of the CNP's exhibited no considerable effect for the presence of NaN_3/DOG except CNP SO_3H. A representative confocal study was performed to visualize the entry of CNPs and corroborated the cell viability results in primary breast cancer cells. It was found that using CNP PEG_{10K} and CNP SO_3H could enter to a higher extent in MCF-7 cells, presumably through more than one endocytic routes *i.e.* clathrin- and energy-dependent pathways as previously demonstrated by our MTT assay (Figure 3.12). Pristine CNPs were shown to significantly enter the MCF-7 cells although being non-responsive

to any of the used inhibitors under investigation. It clearly indicated a non-specific internalization route for MCF-7 cells. On the contrary, in case of CNP SH, no significant level of nanoparticle fluorescence (green) was noticed inside the cells. We may conclude that while cellular internalization of PEG and sulfonate functionalities get facilitated *via* specific endocytic routes, CNP presenting thiols on their surface greatly diminish the entry in early stage breast cancer cells.

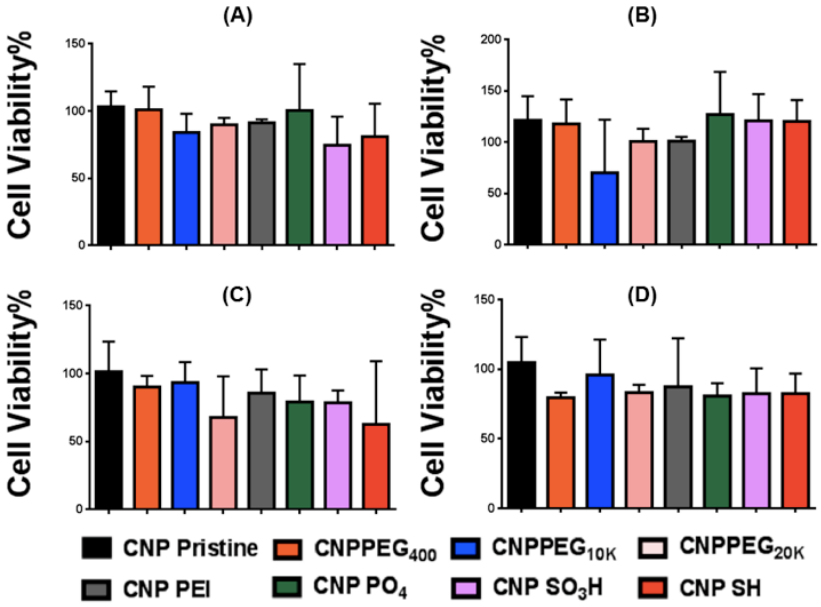

Figure 3.10 Cell viability of different nanoparticle formulations in the presence of endocytic inhibitors is shown. MCF-10A cells (10,000 per well) were plated in 96 well plates for 24h before performing the treatment. Cells were first incubated with different endocytic inhibitors, (A) NaN_3/DOG at 37°C, (B) chlorpromazine, (C) dynasore, (D) nystatin for 1h followed by the addition of CNPs. Experiments were performed in triplicates. Statistical analysis was performed using One-way ANOVA where CNP Pristine was taken as the control column and compared with other nanoparticles. Cell viability of the nanoparticles was plotted as Mean±Standard Deviation, N=3 and * means $p<0.05$, ** means $p<0.01$, *** means $p<0.001$ and **** means $p<0.0001$.

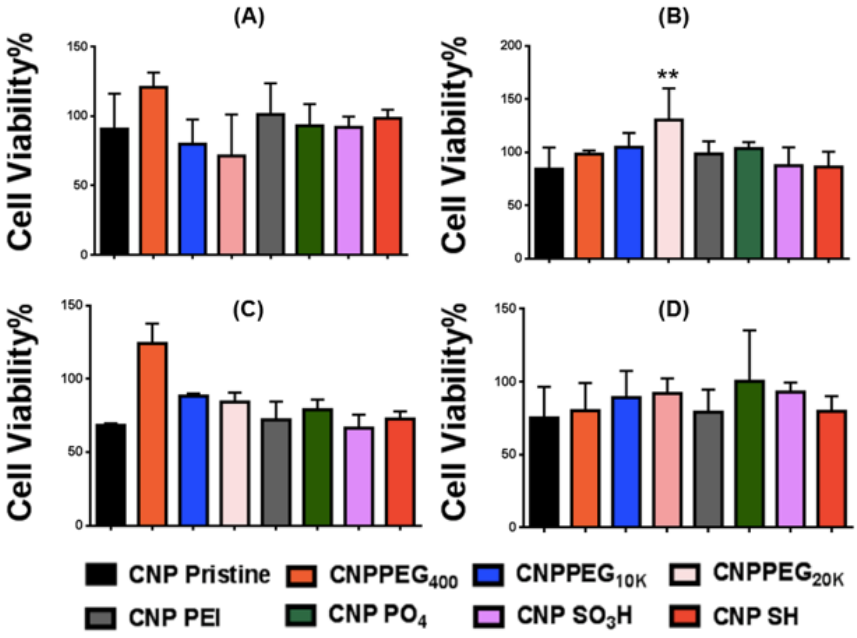

Figure 3.11 Cell viability of different nanoparticle formulations in presence of endocytic inhibitors is shown. MCF-7 cells (10000 per well) were plated in 96 well plates for 24h before performing the treatment. Cells were first incubated with different endocytic inhibitors, (A) NaN_3/DOG at 37°C, (B) chlorpromazine (C) dynasore (D) nystatin for 1h followed by the addition of CNP formulations. Experiments were performed in triplicates. Statistical analysis was performed using One-way ANOVA where CNP pristine was taken as the Control column and compared with other nanoparticle formulations. Cell viability of the nanoparticle formulations was plotted as Mean± Standard Deviation, N=3 and * means $p<0.05$, ** means $p<0.01$, *** means $p<0.001$ and **** means $p<0.0001$.

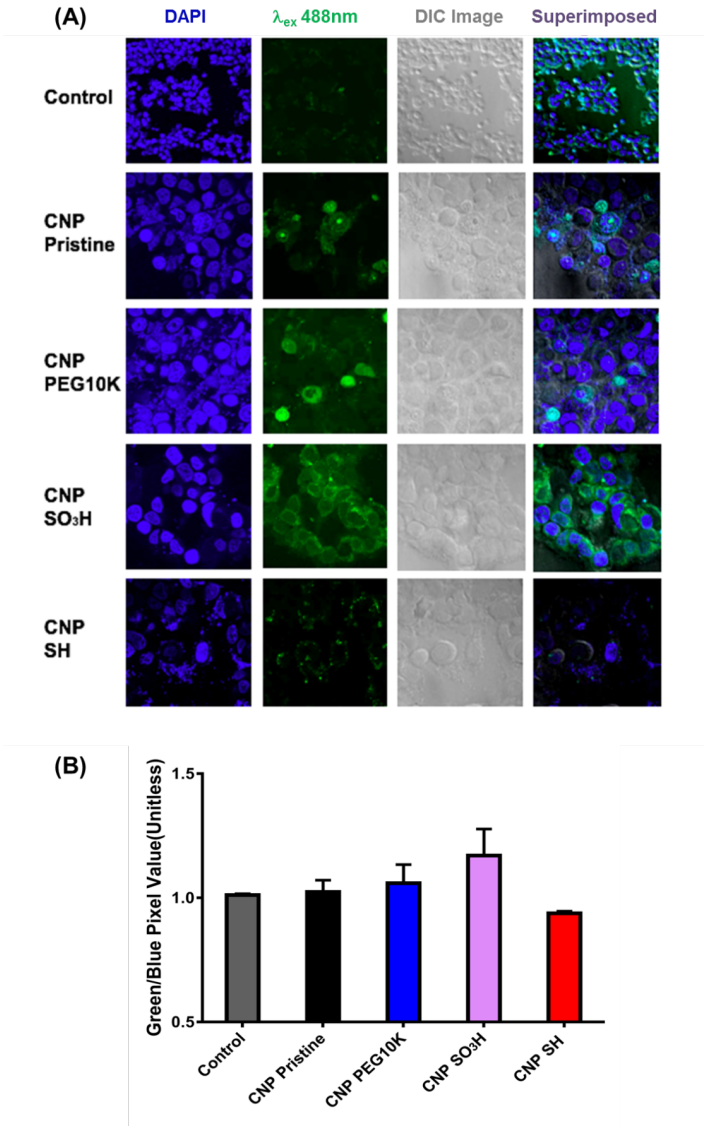

Figure 3.12 (A) Fluorescence confocal microscopy images of MCF-7 cells (1) untreated or (2) treated with CNP Pristine, CNP PEG10K, CNP SO_3H and CNP SH. Confocal images studied under (A) fluorescence with DAPI, (B) CNPs excited at 488 nm, (C) DIC images and (D) superimposed images; and (B) analysis of confocal images using ImageJ and calculating the green pixel / blue pixel ratio.

For the late stage breast cancers, representative MDA-MB231 cells were used to reveal the prominence of lipid-raft mediated pathway for CNPs irrespective of their surface charge or particle size. [40] MDA-MB-231 is an invasive, estrogen-independent, late-stage metastatic and well-differentiated breast cancer cells. Interestingly, pristine CNP did not respond to either lipid-raft mediated pathway or any of the other investigated pathways. (Figure 3.13) This behavior is in sharp contrast with the early stage breast cancer cells. Among various PEGylated CNPs, CNP PEG_{400} showed a higher tendency for cell uptake *via* lipid-raft mediated path. This observation was presumably due to a better association of lower molecular weight PEG with lipid raft although further dedicated studies would be required to confirm this. The presence of phosphate groups relied mostly on lipid-raft mediated pathway, while no such selectivity was seen for CNP SO_3H (negative). It was also found that positively charged CNPs entered the cells through a lipid-raft mediated pathway. A pronounced cell uptake could be achieved at low temperature of 4°C for PEGylated CNP's with an exception of CNP $PEG_{10K.}$

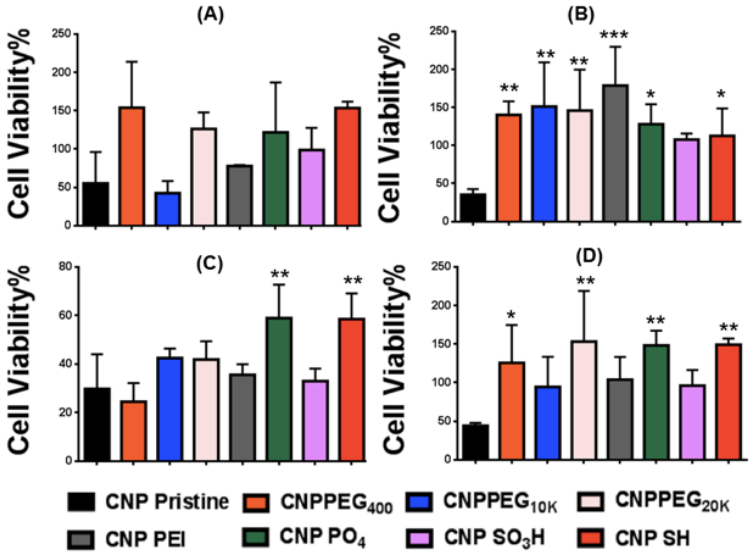

Figure 3.13 Cell viability of different nanoparticle formulations in presence of endocytic inhibitors is shown. MDA-MB231 cells (10,000 per well) were plated in 96 well plates for 24h before performing the treatment. Cells were first incubated with different endocytic inhibitors, (A) NaN_3/DOG at 37°C, (B) chlorpromazine, (C) dynasore, (D) nystatin for 1h followed by addition of CNPs. Experiments were performed in triplicates. Statistical analysis was performed using One-way ANOVA where CNP Pristine was taken as the Control column and compared with other nanoparticles. Cell viability of the nanoparticle formulations was plotted as Mean± Standard Deviation, N=3 and * means $p<0.05$, ** means $p<0.01$, *** means $p<0.001$ and **** means $p<0.0001$.

For scenario of metastatic cancer, BT-549, a representative triple negative cell line was selected from a papillary, invasive ductal tumor which is originally known to metastasize to three of seven regional lymph nodes. We noticed that pristine CNP entered the cells *via* clathrin mediated pathway while high M_w PEGylated CNPs (CNP PEG_{10K} and CNP PEG_{20K}) followed multiple endocytic pathways for entry. (Figure 3.14) Interestingly, smaller pegylated CNPs followed

energy dependent pathway. It was observed that positively charged CNPs could internalize metastatic breast cancer cells through clathrin- and dynamin-dependent pathway, whereas negatively charged CNPs did not show any specific trends for entry. While CNP SH did not show any significant variation *via* investigated pathways similar to primary and advanced stage breast cancer cells.

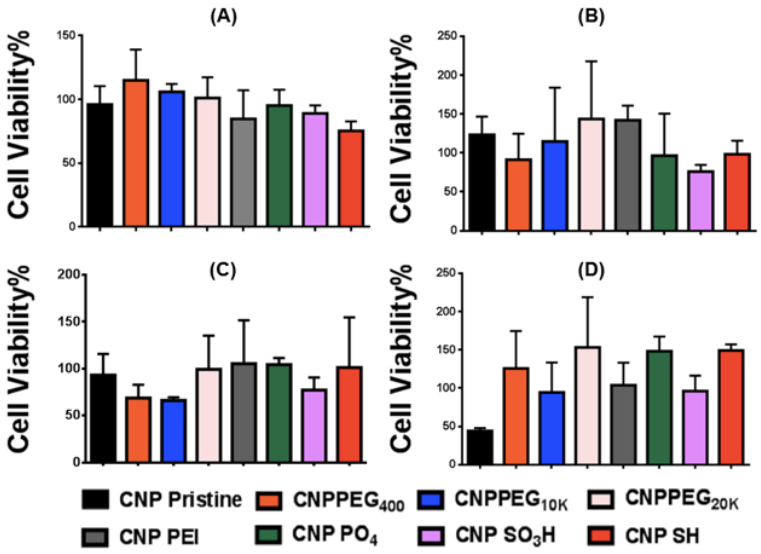

Figure 3.14 Cell viability of different Nanoparticle formulations in presence of endocytic inhibitors is shown. BT-549 cells (10000 per well) were plated in 96 well plates for 24hrs before performing the treatment. Cells were first incubated with different endocytic inhibitors, (A) NaN_3/DOG at 37°C, (B) chlorpromazine, (C) dynasore, (D) nystatin for 1h followed by addition of CNP formulations. Experiments were performed in triplicates. Statistical analysis was performed using One-way ANOVA where CNP Pristine was taken as the Control column and compared with other Nanoparticle formulations. Cell viability of the nanoparticle formulations was plotted as Mean±Standard Deviation, N=3 and * means $p<0.05$, ** means $p<0.01$, *** means $p<0.001$ and **** means $p<0.0001$.

Table 3.3 Analysis of cellular internalization of CNPs via NaN_3/DOG at 4°C (ATP depletion and slowing down of metabolism) by comparing it with NaN_3/DOG at 37°C (ATP depletion alone). Each of the CNPs were analyzed using power analysis and mean fold increase ≥ 1.35 was considered to be significant and designated by '+' and mean fold increase < 1.35 was designated as '- ', meaning no significant inhibition.

Nanoparticle	MCF-7	MDA-MB231	BT-549
CNP Pristine	-	-	-
CNP PEG400	-	+	+
CNP PEG10K	+	-	+
CNP PEG20K	-	+	+
CNP PEI	-	+	-
CNP PO_4	-	-	-
CNP SO_3H	+	-	-
CNP SH	-	-	-

3.4 MECHANISMS OF CELLULAR ENTRY IN MIXED POPULATION OF DIFFERENT STAGED CANCER CELLS

We realize that in practice, tumors would be represented more realistically by studying a heterogeneous mixture of cancer cell population of different stages. Towards this aim, the first phase of study was repeated with heterogeneous mixtures of MCF-7 and MDA-MB231 cells in different ratios of number/number, *i.e.* 25:75, 50:50 and 75:25, respectively. For a 50:50 mixture of MCF-7 and MDA-MB231 cells, pristine CNPs predominantly followed clathrin-mediated pathway for entry while PEGylated CNPs, utilized a combination of all the investigated pathways for entry. CNP SO_3H followed a combination of clathrin-mediated, dynamin

dependent and lipid-raft mediated pathway entry, unlike CNP PO_4, which followed both energy dependent and lipid-raft mediated route for entry. Finally, CNP SH showed to favor all the investigated routes for internalization (Figure 3.18). The effect on cell morphology and density for CNPs, after inhibitor treatment, was also obtained *via* bright field imaging (Figure 3.15). Interestingly for a mixture of MCF-7 and MDA-MB231 in the ratio of 25:75 (% number), we observed (Figure 3.16) that pristine CNP used energy-dependent, dynamin dependent and lipid-raft mediated pathway which also involved energy dependent path for entry to higher population ratio of MCF-7 in mixed population of MCF-7 and MDA-MB231 (75:25) (Figure 3.17). In the mixture of 50:50, it was only responsive to clathrin-mediated entry and non-responsive to other modes of entry. So, an increase in the percentage of well-differentiated MDA-MB231 (or decrease of early stage MCF-7) cell population might have led to a change in endocytic route for entry of bare CNPs. For PEGylated CNPs, CNP PEG_{400} showed to follow all the investigated pathway for entry, whereas CNP PEG_{10K} used both dynamin-dependent and lipid-raft mediated entry in mixed cells with 25:75 and 75:25 population ratio, it followed all the investigated pathways for 50:50 ratios. To analyze the effect a particular inhibitor play in endocytosis of different CNPs in cancer cell lines of different stages, Figure 3.19-Figure 3.22 were plotted. In case of cationic CNPs, CNP PEI was seen to follow all the investigated pathways for internalization in the cells. For anionic CNPs, all the investigated pathways were generally found to be activated in mixture with high MCF-7 population while the presence of high MDA-MB231 dictates the anionic CNPs cellular entry through lipid-raft. Thus, overall, the presence of MDA-MB231 cell population dominated the internalization pathway of CNPs irrespective of their size and surface chemistry.

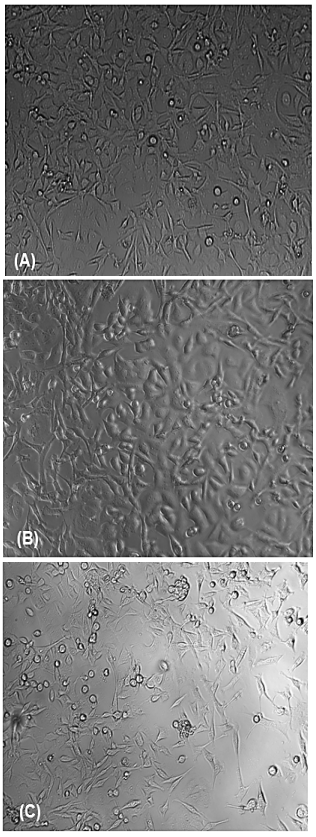

Figure 3.15 Bright field images of MCF-7 and MDA-MB231 cells mixed in 50:50 ratio (A) untreated (B) treated with inhibitor for 1 h, followed by additional incubation with CNP formulations (C), having a concentration of 5% v/v for 48h. 8000 cells were plated in 96 well plates for 24h before performing the inhibitor treatment. Experiments were done in triplicates.

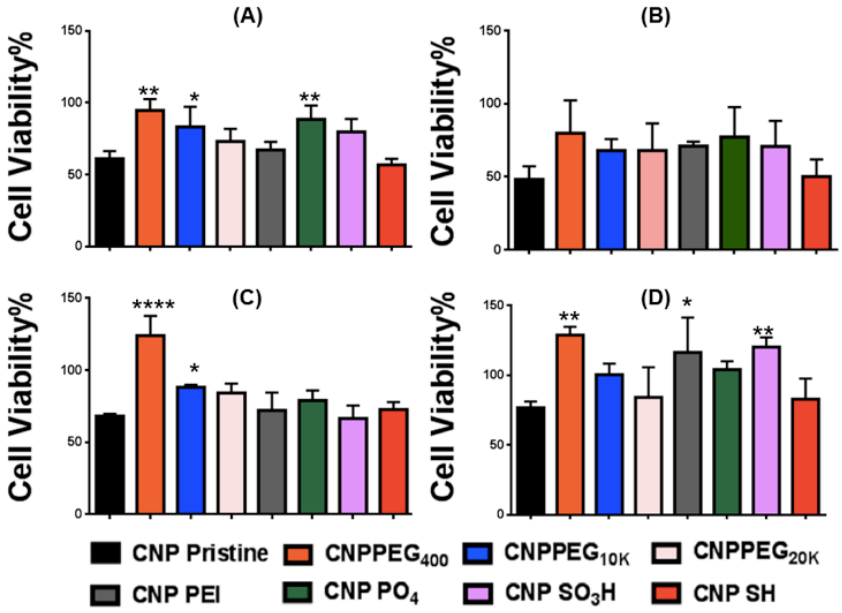

Figure 3.16 Cell viability of different nanoparticle formulations in presence of different endocytic inhibitors is shown. A mixture of MCF-7 and MDA-MB231 cells (8,000 cells per well) in the ratio of 25:75 (v/v) were plated in 96 well plates for 24h before performing the treatment. Cells were first incubated with different endocytic inhibitors, (A) NaN_3/DOG at 37°C, (B) chlorpromazine (C) dynasore (D) nystatin for 1 h followed by addition of CNPs. Experiments were performed in triplicates. Statistical analysis was performed using One-way ANOVA where CNP pristine was taken as the control column and compared with other Nanoparticle formulations. Cell viability of the nanoparticles was plotted as Mean± Standard Deviation, N=3 and * means $p<0.05$, ** means $p<0.01$, *** means $p<0.001$ and **** means $p<0.0001$.

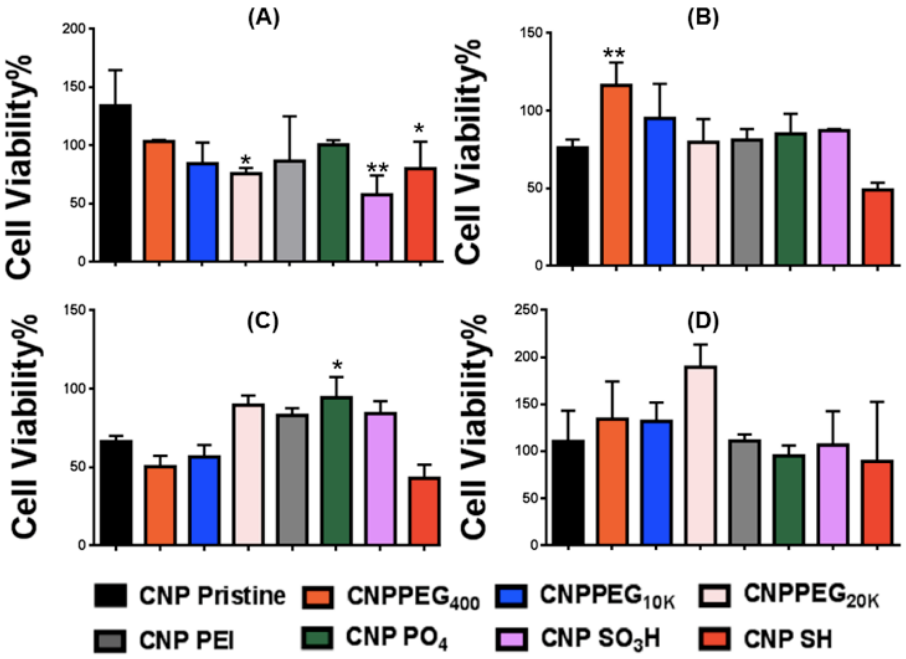

Figure 3.17 Cell viability of different nanoparticle formulations in presence of different endocytic inhibitors is shown. A mixture of MCF-7 and MDA-MB231 cells (8,000 cells per well) in the ratio of 75:25 (v/v) were plated in 96 well plates for 24h before performing the treatment. Cells were first incubated with different endocytic inhibitors, (A) NaN_3/DOG at 37°C, (B) chlorpromazine (C) dynasore (D) nystatin for 1 h followed by addition of CNPs. Experiments were performed in triplicates. Statistical analysis was performed using One-way ANOVA where CNP pristine was taken as the control column and compared with other Nanoparticle formulations. Cell viability of the nanoparticles was plotted as Mean± Standard Deviation, N=3 and * means $p<0.05$, ** means $p<0.01$, *** means $p<0.001$ and **** means $p<0.0001$.

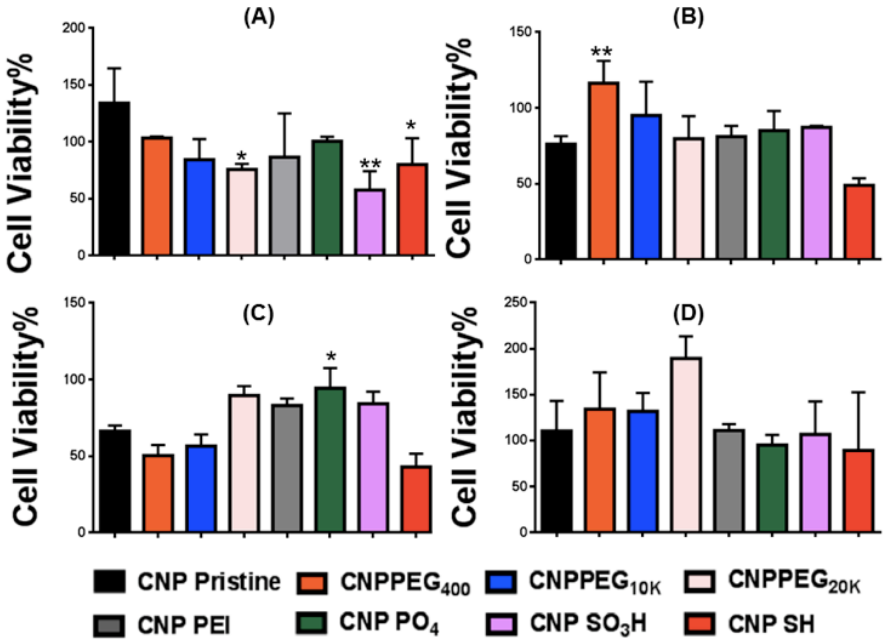

Figure 3.18 Cell viability of different nanoparticle formulations in presence of different endocytic inhibitors is shown. A mixture of MCF-7 and MDA-MB231 cells (8,000 cells per well) in the ratio of 50:50 (v/v) were plated in 96 well plates for 24h before performing the treatment. Cells were first incubated with different endocytic inhibitors, (A) NaN_3/DOG at 37°C, (B) chlorpromazine (C) dynasore (D) nystatin for 1 h followed by addition of CNPs. Experiments were performed in triplicates. Statistical analysis was performed using One-way ANOVA where CNP pristine was taken as the control column and compared with other Nanoparticle formulations. Cell viability of the nanoparticles was plotted as Mean± Standard Deviation, N=3 and * means $p<0.05$, ** means $p<0.01$, *** means $p<0.001$ and **** means $p<0.0001$.

All the results obtained from inhibitor studies were in terms of cell viability (Figure 3.10- Figure 3.14). So to get information about the internalization of these CNPs in cancer cells lines, they have to be converted to fold increases values first, which are shown below.

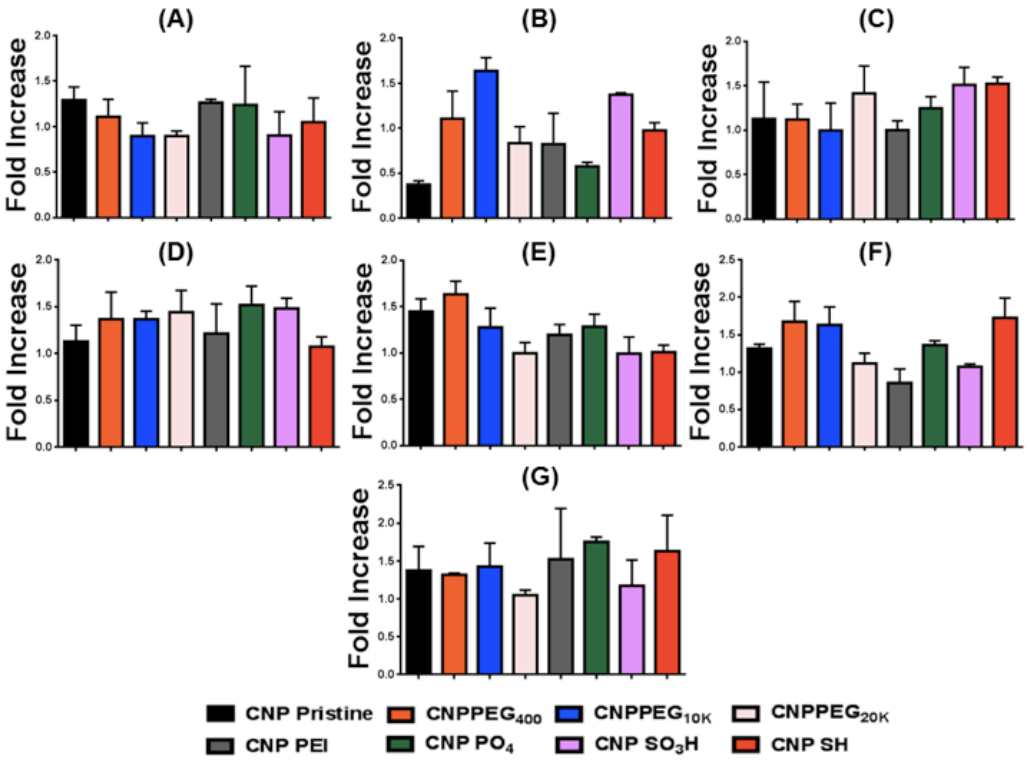

Figure 3.19 MTT assay for evaluation of inhibitor efficiency of NaN_3/DOG (at 37°C) for different CNP formulations (5% v/v) in (A) MCF-10a, (B) MCF-7, (C) MDA-MB231, (D) BT-549, (E) 25:75 mixtures of MCF: MDA-MB231 (F) 50:50 mixtures of MCF: MDA-MB231 (G) 75:25 mixtures of MCF: MDA-MB231 was done, consequently from which fold increase was obtained. A non-synchronized population of cells (10,000 or 8,000 cells per well) was plated in 96 well plates for 24h before performing the treatments. Cells were first incubated with inhibitor, NaN_3/DOG (10mM/50 mM) for 1h followed by CNP addition. Experiments were performed in triplicates. Fold Increase ≥ 1.35 was considered to be significant.

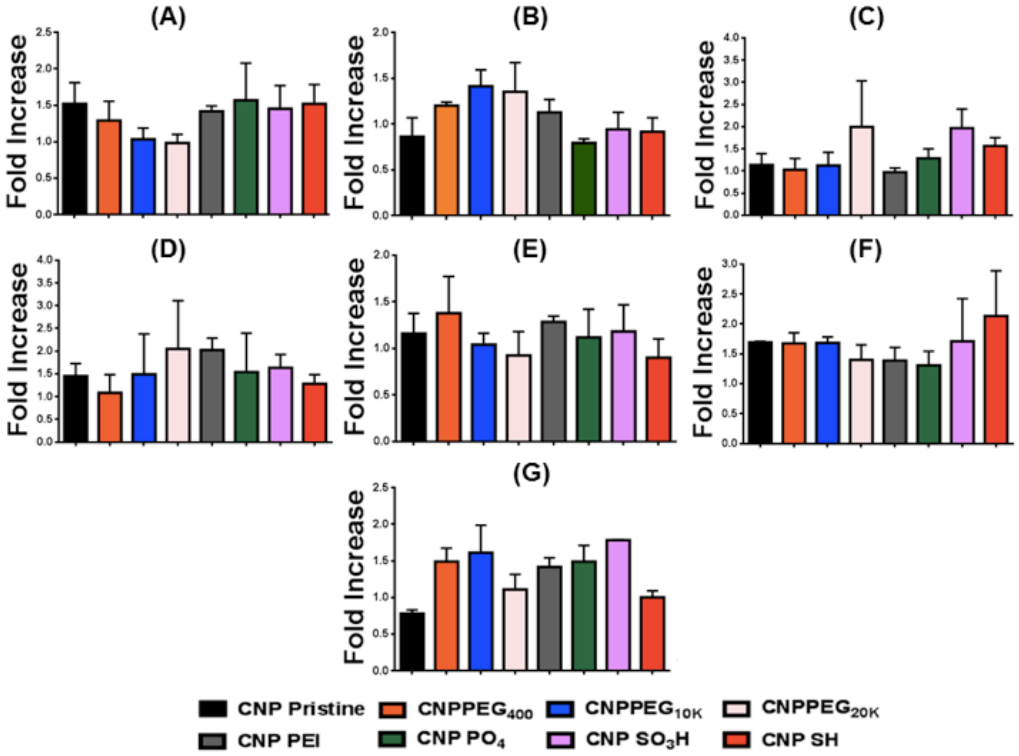

Figure 3.20 MTT assay for evaluation of inhibitor efficiency of chlorpromazine (CPM) (at 37°C) for different CNP formulations (5% v/v) in (A) MCF-10a, (B) MCF-7, (C) MDA-MB231, (D) BT-549, (E) 25:75 mixtures of MCF: MDA-MB231 (F) 50:50 mixtures of MCF: MDA-MB231 (G) 75:25 mixtures of MCF: MDA-MB231 was done, consequently from which fold increase was obtained. A non-synchronized population of cells (10,000 or 8,000 cells per well) was plated in 96 well plates for 24h before performing the treatments. Cells were firstly incubated with inhibitor, NaN_3/DOG (10mM/50 mM) for 1h followed by CNP addition. Experiments were performed in triplicates. Fold Increase ≥ 1.35 was considered to be significant.

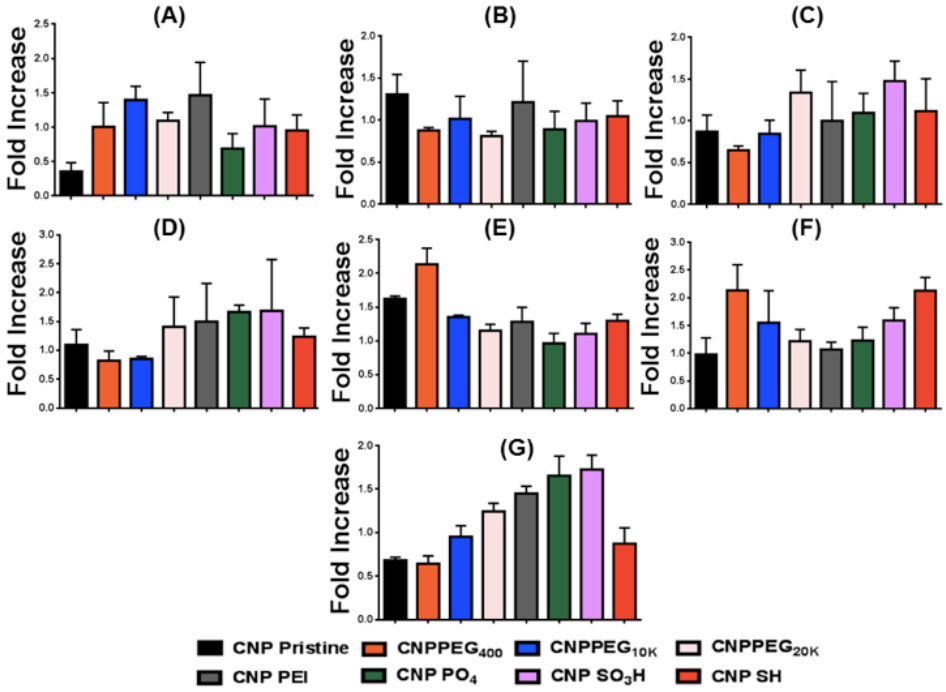

Figure 3.21 MTT assay for evaluation of inhibitor efficiency of dynasore (at 37°C) for different CNP formulations (5% v/v) in (A) MCF-10a, (B) MCF-7, (C) MDA-MB231, (D) BT-549, (E) 25:75 mixtures of MCF: MDA-MB231 (F) 50:50 mixtures of MCF: MDA-MB231 (G) 75:25 mixtures of MCF: MDA-MB231 was done, consequently from which fold increase was obtained. A non-synchronized population of cells (10,000 or 8,000 cells per well) was plated in 96 well plates for 24h before performing the treatments. Cells were first incubated with inhibitor, NaN_3/DOG (10mM/50 mM) for 1h followed by CNP addition. Experiments were performed in triplicates. Fold Increase ≥ 1.35 was considered to be significant.

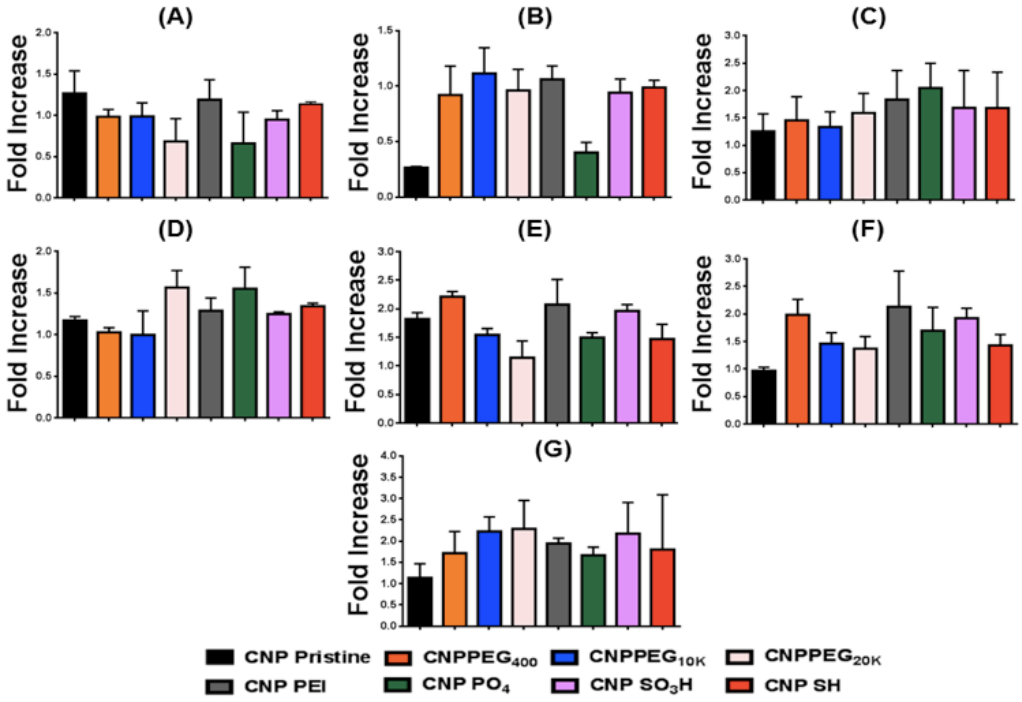

Figure 3.22 MTT assay for evaluation of inhibitor efficiency of nystatin (at 37°C) for different CNP formulations (5% v/v) in (A) MCF-10a, (B) MCF-7, (C) MDA-MB231, (D) BT-549, (E) 25:75 mixtures of MCF: MDA-MB231 (F) 50:50 mixtures of MCF: MDA-MB231 (G) 75:25 mixtures of MCF: MDA-MB231 was done, consequently from which fold increase was obtained. A non-synchronized population of cells (10,000 or 8,000 cells per well) was plated in 96 well plates for 24h before performing the treatments. Cells were firstly incubated with inhibitor, NaN_3/DOG (10mM/50 mM) for 1h followed by CNP addition. Experiments were performed in triplicates. Fold Increase ≥ 1.35 was considered to be significant.

The mode of endocytosis entry of CNPs could be corroborated with cell viability results by creating a heat map. (Figure 3.23) A mean fold-increase value greater than or equal to 1.35 was considered to have significant uptake inhibition and suggested the role of predominant

internalization route. These fold-increase values would lie on a higher confidence interval (~ 95%), as calculated by confidence interval calculator by Mccallum-layton, thereby making subsequent comparison amongst rest of data sets significant.

It was observed that endocytic entry in late stage breast cancer (MDA-MB231) cells followed a lipid-raft pathway irrespective of the size and surface chemistry. Interestingly, in metastatic cells (BT-549) most of the particles followed a combination of two or more pathways for internalization, thereby leading to a higher likelihood of internalization of the nanoparticles. However, for early stage breast cancer (MCF-7) cells, no such general trend was observed. Furthermore, for heterogeneous mixture of MCF-7 and MDA-MB231 cells, it was observed that all tested endocytic uptake routes were active, thereby allowing CNPs to internalize *via* multiple endocytic pathways, a trend which was not followed by most of the CNPs in either MCF-7 or MDA-MB231 cells alone. In addition, it could be concluded that as the cancer progresses from early to metastatic stage *via* late-stage, anionic CNPs and neutral CNPs enter the cells more predominantly compared to cationic CNPs. (Figure 3.24)

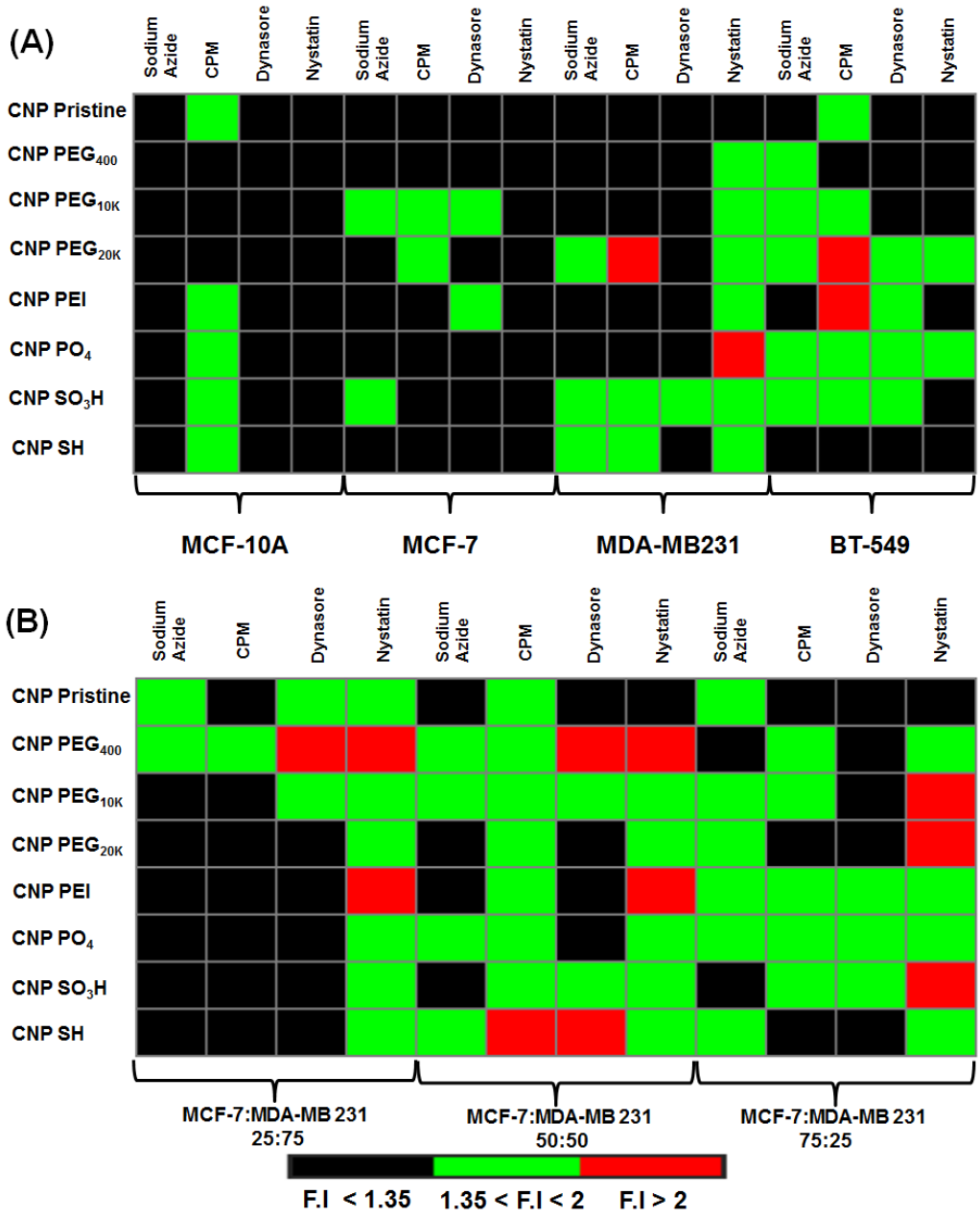

Figure 3.23 Heat map analysis to show the effect of Inhibitors on uptake of CNPs for different breast cancer cell lines was plotted. Fold Increase values between 1.35-2.0 (green) and greater than 2 (red) were considered as significant inhibitor in uptake, whereas Fold increase values less than 1.35 were considered to be insignificant inhibition in uptake.

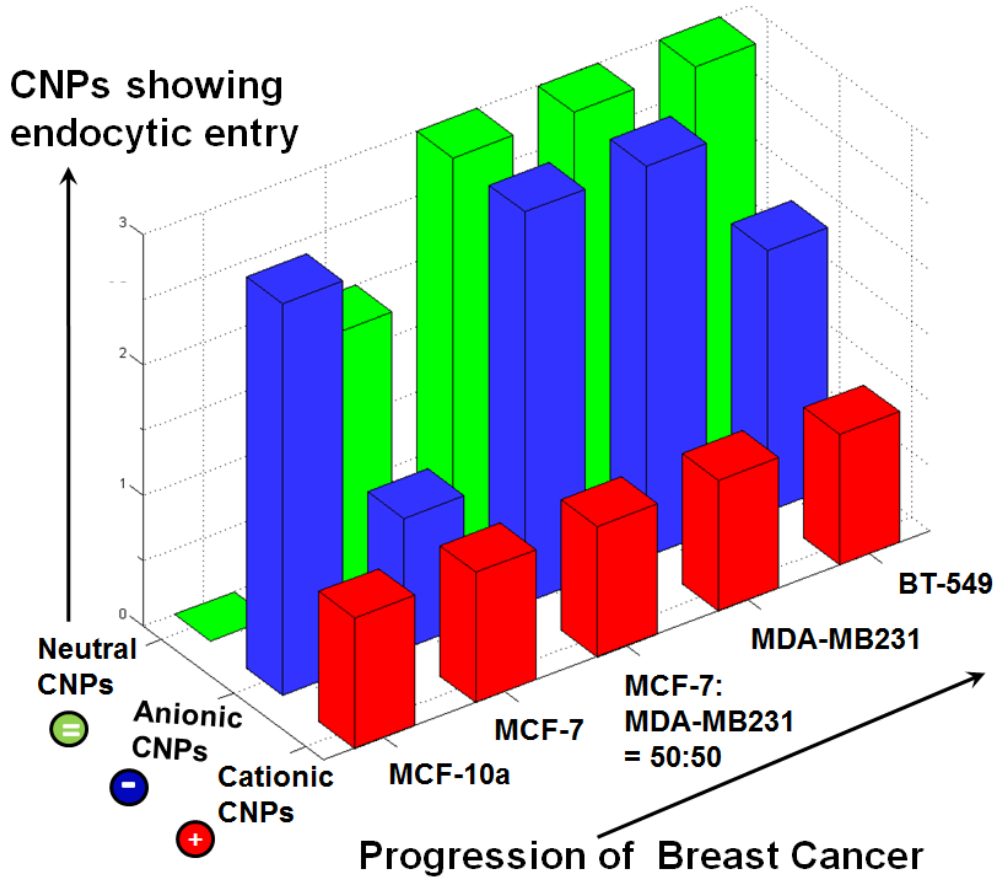

Figure 3.24 Parametric evaluation of surface charge and progression of breast cancer effects on internalization of CNPs. As the cancer progresses from initial stages to metastatic, more number of anionic and neutral CNPs show more tendency for internalization *via* endocytic routes.

CHAPTER 4

CONCLUSION AND FUTURE OUTLOOK

4.1 CURRENT PERSPECTIVE

Herein, we have reported a systematic synthesis of sub 50nm carbon nanoparticles (CNP) presenting neutral, anionic, and cationic surface headgroups. A subset of CNPs with ~ 10, 20, and 40nm hydrodynamic sizes are synthesized with neutral surface headgroups. Comprehensive physiochemical characterizations were performed to confirm the successful synthesis of these nanoplatforms. The cellular internalization of these CNPs was systematically quantified for the first time in various stages of breast cancer cells (early, late and metastatic), providing a parametric assessment of charge and size effects. Distinct activities are noticed with these systems as they interact with various stages of the cancer cells.

The main findings can be summarized as follows:

- Distinct activities are noticed with these nanoparticles based systems as they interact with various stages of cancer cells in a different way. For late stage cancer cells (represented using MDA-MB231cells), lipid raft mediated endocytosis route was predominant, whereas for metastatic cancer cells (represented using BT-549cells), a combination of clathrin-mediated and energy dependent pathways were responsible for the internalization. However, in case for non-tumorigenic cells (represented by MCF 10a cells), clathrin-mediated entry was observed.
- Our results indicated that a metastatic breast cancer could be targeted with a nanosystem

presenting anionic phosphate groups or pegylated group having a molecular weight of 20K Da. On the contrary, for patients with late stage cancer, drugs could be delivered with sulfonate functionalized carbon nanoparticles with higher probability of intracellular transport.

4.2 FUTURE OUTLOOK

One of the key translational challenges has been to better stratify nanotherapeutics based on patients' pathophysiologic information collected from biopsy. This work takes an exactitude nanomedicine approach to predict how well drug-loaded nanoparticles will accumulate in a particular tumor.

REFERENCES

[1] M. Ferrari, *Nature Reviews Cancer.***2005**, 5,161

[2] Youan BB, *Nanomedicine.***2008**, 3(4),401

[3] O.C. Farokhzad, R. Langer, *ACS Nano*.**2009**, 3(1),16

[4] I. Brigger, C. Dubernet, P. Couvreur, *Advanced Drug Delivery Reviews*. **2012**, 64, 24

[5] T. Wang, J. Bai, X. Jiang, G.U. Nienhaus, *ACS Nano*. **2012**, 6(2), 1251.

[6] D. Vercauteren, R.E. Vandenbroucke, A.T. Jones, J. Rejman, J. Demeester, S.C. De Smedt, N.N. Sanders, K. Braeckmans, *Molecular Therapy*. 2010, 18(3), 561.

[7] X. Chen, F. Tian, X. Zhang, W. Wang, *Soft Matter*. **2013**, 9, 7592.

[8] G.J. Doherty, H.T. McMahon, *Annual Reviews of Biochemistry*. **2009**, 78, 857.

[9] A.I. Ivanov*, Methods in Molecular Biology*. **2008**, 440, 15.

[10] S.D. Conner, S.L. Schmid*, Nature*. **2003**, 422, 37.

[11] J.A. Swanson, C. Watts, Trends in Cell Biology. 1995, 5, 424

[12] S. Kumari, M.G. Swetha, S. Mayor, *Cell Research*. **2010**, 20, 256.

[13] M. Lundqvist, J. Stigler, G. Elia, I. Lynch, T. Cedervall, A.K. Dawson, *Proceeding of National Academy of Sciences, USA*. **2008**, 105, 14265.

[14] S.L. Zhang, J. Li, G. Lykotrafitis, G. Bao, S. Suresh, *Advanced Material*s. **2009,** 21, 419.

[15] C.D. Walkey, J.B. Olsen, H. Guo, A. Emill, W.C.W. Chan, *Journal of American Chemical Soceity*. **2012**, 134(4), 2139.

[16] K. Saha, S.T. Kim, B. Yan, O.R. Miranda, F.S. Alfonso, D. Shlosman, V.M. Rotello, *Small*. **2013**, 9(2), 300.

[17] K. Kostarelos, L. Lacerda, G. Pastorin, W. Wi, S. Wieckowski, J. Luangsivilay, S. Godefroy, D. Pantarotto, J.P. Briand, S. Muller, M. Prato, A. Bianco, *Nature Nanotechnolgy*, **2007**, 2, 108.

[18] M. Liang, I.C. Lin, M.R. Whittaker, R.F. Minchin, M.J. Monteiro, I. Toth, *ACS Nano*. **2010**, 4, 403.

[19] R.R. Arvizo, S. Rana, O.R. Miranda, R. Bhattacharya, V.M. Rotello, P. Mukherjee, *Nanomedicine*. **2011**, 7, 580.

[20] E.C. Cho, J.W. Xie, P.A. Wurm, Y.N. Xia, *Nano Letters*. **2009**, 9, 1080.

[21] Z. Liu, X.J. Liang, *Theranostic*. **2012**, 2(3), 235.

[22] W. Qin, D. Ding, J. Liu, W.Z. Yuan, Y. Hu, B. Liu, B.Z. Tang, *Advanced Functional Materials*. **2011**, 22(4), 771.

[23] S.K. Misra, H.H. Chang, P. Mukherjee, S. Tiwari, A. Ohoka, D. Pan, *Scientific Reports*. **2015**, 5, 14986.

[24] A.C. Ferrari, J. Roberston, *Philosphical Transactions of the Royal Society A*. **2004**, 362, 2477.

[25] R. Mahou, C. Wandrey, *Polymers*. 2012, 4, 561.

[27] M. Gliem, W-M. Heupel, V. Spindler, G.S. Harms, J. Waschke, *American Journal of Physiology – Cell Physiology*. **2010**, 299(3), 606.

[28] E.A. Papakonstanti, C. Stournaras, FEBS Letters. 2008, 582(14), 2120.

[29] C. Allen, Y. Yu, A. Eisenberg, D. Maysinger, *Biochim. Biophy. Acta*. **1999**, *1421*, 32.

[30] L. Wang, Y. Liu, W. Li, X. Jiang, Y. Ji, X. Wu, L. Xu, Y. Qiu, K. Zhao, T. Wei, Y. Li, Y. Zhao, C. Chen, *Nano Letters.* **2011**, 11(2), 772.

[31] J.S. Kim, T. J. Yoon, K. N. Yu, M.S. Noh, M. Woo, B. G. Kim, K. H. Lee, B.H. Sohn, S.B. Park, J.K. Lee, M.H. Cho, *Journal of Veterinary Science*. **2006**, 11, 772.

[32] L.H. Wang, K.G. Rothberg, R.G. Anderson, *Journal of Cell Biology*. **1993**, 123(5), 1107.

[33] H.T. Mc Mahon, E. Boucrot, *Nature Reviews Molecular Cell Biology*. **2011**, 12, 517.

[34] A.D. Stuart, T.D.K. Brown, *Journal of Cell Virology*. **2006**, 80(15), 7500.

[35] E. Macia, M. Ehrlich, R. Massol, E. Boucrot, C. Bruneer, T. Kirchhausen, *Development Cell*. **2006**, 10(6), 839.

[36] T. Kirchhausen, E. Macia, H. E. Pelish, *Methods in Enzymology*. **2008**, *438*, 77.

[37] Y. Chen, S. Wang, X. Lu, H. Zhang, Y. Fu, Y. Luo, *Blood*. **2011**, 117, 6392.

[38] J.S. Sigismund, T. Woelk, C. Puri, E. Maspero, C. Tacchetti, P. Transidico, P. P. Di Fiore, S. Polo, *Proceeding of National Academy of Sciences, U.S.A.* **2005**, *102*, 2760.

[39] H.Raghu, P. K. Sodadasu, R. R. Malla, C. S. Gondi, N. Estes, J.S. Rao, *BMC Cancer*. **2010**, 10, 647.